Monthly Notices
of the
ROYAL ASTRONOMICAL SOCIETY

MNRAS **440,** 631–651 (2014)
Advance Access publication 2014 March 12

doi:10.1093/mnras/stu286

Modelling the alumina abundance of oxygen-rich evolved stars in the Large Magellanic Cloud

O. C. Jones,[1]★ F. Kemper,[2] S. Srinivasan,[2] I. McDonald,[1] G. C. Sloan[3] and A. A. Zijlstra[1]

[1]*Jodrell Bank Centre for Astrophysics, School of Physics & Astronomy, Alan Turing Building, The University of Manchester, Oxford Road, Manchester M13 9PL, UK*
[2]*Institute of Astronomy and Astrophysics, Academia Sinica, 11F ASMAB, NTU, No. 1, Sec. 4, Roosevelt Rd, Taipei 10617, Taiwan, Republic of China*
[3]*Department of Astronomy, Cornell University, Ithaca, NY 14853, USA*

Accepted 2014 February 10. Received 2014 February 10; in original form 2013 September 11

ABSTRACT

In order to determine the composition of the dust in the circumstellar envelopes of oxygen-rich asymptotic giant branch (AGB) stars, we have computed a grid of MODUST radiative-transfer models for a range of dust compositions, mass-loss rates, dust-shell inner radii and stellar parameters. We compare the resulting colours with the observed oxygen-rich AGB stars from the SAGE-Spec Large Magellanic Cloud (LMC) sample, finding good overall agreement for stars with a mid-infrared excess. We use these models to fit a sample of 37 O-rich AGB stars in the LMC with optically thin circumstellar envelopes, for which 5–35 μm *Spitzer* infrared spectrograph (IRS) spectra and broad-band photometry from the optical to the mid-infrared are available. From the modelling, we find mass-loss rates in the range $\sim 8 \times 10^{-8}$–$5 \times 10^{-6}\,\mathrm{M}_{\odot}\,\mathrm{yr}^{-1}$, and we show that a grain mixture consisting primarily of amorphous silicates, with contributions from amorphous alumina and metallic iron, provides a good fit to the observed spectra. Furthermore, we show from dust models that the *AKARI* [11]−[15] versus [3.2]−[7] colour–colour diagram is able to determine the fractional abundance of alumina in O-rich AGB stars.

Key words: radiative transfer – stars: AGB and post-AGB – circumstellar matter – dust, extinction – Magellanic Clouds – infrared: stars.

1 INTRODUCTION

Stars on the asymptotic giant branch (AGB) lose a significant fraction of their matter through slow dense winds at rates of 10^{-10}–$10^{-4}\,\mathrm{M}_{\odot}\,\mathrm{yr}^{-1}$ (Bowen & Willson 1991). During this phase of evolution the effective stellar temperature is low enough for molecules to form and dust grains to condense in the circumstellar outflow. In general, dust formation occurs in stages known as the 'dust condensation sequence' and depends on the physical conditions in the envelope (Tielens 1990; Gail & Sedlmayr 1999; Gail 2010). The mineralogy of the dust is dominated by the chemistry of the envelope (which is set by a star's photospheric C/O atomic ratio and initial elemental abundance), and by the envelope's temperature and density (which determine which condensation products are stable).

Although not understood in detail, the thermodynamic condensation sequence for oxygen-rich outflows (C/O < 1) predicts that refractory oxides such as alumina (Al_2O_3) would be the first astrophysically significant species to form. These grains can exist relatively close to the star ($T_{\mathrm{cond}} \sim 1400$ K at pressures relevant to stellar outflows) and may act as seed nuclei for other grains (e.g. Onaka, de Jong & Willems 1989; Stencel et al. 1990; Sogawa & Kozasa 1999). At larger radii, where the temperature is lower ($T \sim 1000$ K), silicate grains form.

It is well established that the dust in oxygen-rich outflows consists mainly of silicates (Woolf & Ney 1969; Hackwell 1972; Treffers & Cohen 1974). However, alumina dust has been detected in the spectra of some low mass-loss rate ($\dot{M}$) O-rich AGB stars in the Milky Way (Onaka et al. 1989; Speck et al. 2000; Dijkstra et al. 2005). These stars show a broad low-contrast emission feature in the 7–14-μm region which is best fitted with a blend of amorphous alumina and amorphous silicates. As the star evolves along the AGB, the shape and peak position of this feature changes; silicate dust becomes more important and dominates the 10-μm emission (Little-Marenin & Little 1990; Sloan & Price 1995). At high mass-loss rates the 10-μm feature is only due to silicates. This sequence has been quantified by Sloan & Price (1995, 1998) using flux ratios in the 9–12-μm region.

The *Spitzer* Space Telescope has taken spectra of a large number of individual evolved stars in the Large and Small Magellanic

★ E-mail: ojones@jb.man.ac.uk

© 2014 The Authors
Published by Oxford University Press on behalf of the Royal Astronomical Society

Downloaded from http://mnras.oxfordjournals.org/ at Cornell University Library on April 16, 2016

Clouds (LMC and SMC, respectively), covering a wide range of colours and magnitudes (Kemper et al. 2010). Although the mineralogy of the oxygen-rich AGB stars in the Magellanic Clouds is dominated by amorphous silicates both at low and high mass-loss rates (Sargent et al. 2010; Riebel et al. 2012), some sources also contain a small fraction of crystalline silicates (Jones et al. 2012). There is an apparent absence of Al_2O_3 in the *Spitzer* spectra of O-AGB stars in the Magellanic Clouds (Sloan et al. 2008), with the 10-μm feature of low-density (low-$\dot{M}$) winds better reproduced by amorphous silicate grains than the expected mixture of Al_2O_3 and silicates. This implies that either alumina dust is depleted in the LMC or that observational biases hinder its detection. However, an extensive systematic study into the Al_2O_3 content of evolved stars in the LMC has not yet been carried out.

In this study, we evaluate the alumina content of oxygen-rich AGB stars in the Magellanic Clouds, by creating a grid of radiative transfer models that explores a range of physical parameters relevant to evolved stars. In Section 2, we describe how the radiative transfer models for the circumstellar dust shell were computed. Colour–colour diagrams (CCD) of the grid of models are presented in Section 3 and will be used to study the alumina dust in a sample of O-rich AGB stars in the Magellanic Clouds in Section 4. Finally, we discuss our results in Section 5 and summarize this study in Section 6.

2 MODELLING THE CIRCUMSTELLAR DUST SHELL

To determine the relative contributions of alumina dust from the spectra of O-rich AGB stars in the LMC, radiative transfer modelling is required to calculate detailed spectra of circumstellar dust shells. In this paper, we use the one-dimensional radiative transfer code MODUST (Bouwman et al. 2000, 2001; Kemper et al. 2001) to evaluate the emergent spectrum from a central star surrounded by a spherically symmetric dust shell. MODUST solves the transfer equations for the basic free parameters such as stellar temperature, chemical composition, grain-size distribution, etc. under the constraint of radiative equilibrium, using a Feautrier-type method (Feautrier 1964). It also allows the user to implement multiple dust shells, each consisting of different dust components with an independent grain-size distribution function. In the following subsections, we will describe the selection of the input parameters adopted in the modelling. A summary of the model input parameters is given in Table 1.

Table 1. Model parameters.

Parameter	Range of values
Star	
Spectral type	M1, M5, M9
$L_\star$ ($L_\odot$)	7000
$T_{\rm eff}$ (K)	3715, 3396, 2667
$R_\star$ ($R_\odot$)	202.3, 242.1, 392.5
Dust shell properties	
$R_{\rm in}$ ($R_\star$)	2.5, 3, 5, 7.5 and 15
$R_{\rm out}/R_{\rm in}$	200
$v_{\rm exp}$ (km s^{-1})	10
Dust-to-gas ratio (Ψ)	1/200
Density profile	$\rho(r) \sim r^{-2}$
$\dot{M}$ ($M_\odot$ yr^{-1})	10^{-10}–10^{-5}
Dust grain properties	
Size distribution	MRN
Grain shape	CDE
$a_{\rm min}$ (μm)	0.01
$a_{\rm max}$ (μm)	1.00
q	3.5
Dust species	References
Amorphous Mg_2SiO_4	Dorschner et al. (1995)
Am. Al_2O_3	Begemann et al. (1997)
	Koike et al. (1995)
Fe	Ordal et al. (1988)

2.1 Model input

2.1.1 Photospheres

The models have been calculated using three different synthetic stellar photospheres for O-rich stars of solar metallicity taken from Fluks et al. (1994). The spectral types of the central star used in the model grid are M1 with an effective stellar temperature ($T_{\rm eff}$) of 3715 K, M5 ($T_{\rm eff}$ = 3396 K) and M9 ($T_{\rm eff}$ = 2667 K). These were chosen to reproduce the range of values expected for O-AGB stars. As luminosity only acts as a scaling factor for the emission and does not affect the spectral shape (Ivezic & Elitzur 1997), a typical luminosity for AGB stars of 7000 $L_\odot$ was assumed, resulting in stellar radii ($R_\star$) for the central star of 202.3, 242.1 and 392.5 $R_\odot$ (respectively).

2.1.2 Dust shell geometry

The dust is assumed to be distributed in a spherical shell with an r^{-2} density distribution, giving rise to a spherically symmetric, time-independent stellar wind with a constant outflow velocity. The lack of silicate absorption features in the spectra of O-rich AGB stars in the LMC sample and the relative weakness of the mid-infrared (IR) flux compared to the flux at 1 μm (Sargent et al. 2010) indicate that these stars typically have optically thin dust shells in the mid-IR, thus limiting the column density along the line of sight. In optically thin dust shells the geometry of the circumstellar shell has little influence on the appearance of the spectral features, as all grains receive approximately the same amount of (near-IR) stellar photons, and absorption of scattered or emitted radiation is minimal due to the decreasing extinction efficiency of the oxygen-rich dust at longer wavelengths. However, the density profile of the dust shell determines the dust mass distribution over temperature, thus affecting the continuum emission levels and feature strengths. For optically thick dust shells, the geometry of the circumstellar dust would significantly influence the shape of the spectral features and would require a more complex treatment of the density distribution.

The inner radius of the dust shell ($R_{\rm in}$) is determined assuming that the dust temperature at this radius is equal to the condensation temperature of the dust species and that

$$T_{\rm d}(r) = T_\star \left(\frac{R_\star}{2r}\right)^{2/(4+s)}, \quad (1)$$

with $s \approx 1$ (Olofsson 2004). For amorphous silicates, the condensation temperature is $T_{\rm cond} \sim 1000$ K (Gail & Sedlmayr 1999); however, alumina is expected to condense at higher temperatures $T_{\rm cond} \sim 1400$ K. To be consistent with other modelling efforts (e.g. Heras & Hony 2005; Groenewegen 2006; Sargent, Srinivasan & Meixner 2011; Srinivasan, Sargent & Meixner 2011), we do not include multiple dust shells with separate dust components, each

Downloaded from http://mnras.oxfordjournals.org/ at Cornell University Library on April 16, 2016

with its own temperature distribution. Instead, to account for this range in condensation temperature, and for dynamical effects such as pulsations, $R_{\rm in}$ is varied for a best fit. We calculate models for $R_{\rm in} = 2.5$, 3, 5, 7.5 and 15 $R_\star$. These are similar to the range of $R_{\rm in}$ values explored by the O-rich Grid of red supergiant and AGB Models (GRAMS; Sargent et al. 2011), based on estimates for the condensation radius by Höfner (2007).

In some instances, a given set of model parameters may result in dust temperatures at the inner regions of the shell that are in excess of the condensation temperature. We deem these models to be unphysical and eliminate them from our grid.

The outer radius ($R_{\rm out}$) determines the duration of the mass-loss and hence the total shell mass, and increases the amount of cold dust. In order to accurately determine the thickness of the shell, far-IR data are required. The dust temperatures at the outermost regions of the wind only contribute slightly to the mid-IR flux and hence cannot be constrained by our models. For instance, for the M9III model with $R_{\rm in} = 7.5$ and a total mass-loss rate of 1×10^{-6} M$_\odot$ yr^{-1}, the 24-μm flux was only ∼4.8 per cent higher for $R_{\rm out} = 1000\,R_{\rm in}$ as compared to $R_{\rm out} = 200\,R_{\rm in}$. Thus, we used a fixed value of $R_{\rm out} = 200\,R_{\rm in}$ as a lower limit for the shell thickness, as this is computationally less expensive.

The outflow dynamics, and in particular the density and velocity of the wind, play an important role in the emergent spectra. Typical wind velocities derived from observations of Galactic AGB stars range from 10 to 20 km s^{-1} (Vassiliadis & Wood 1993; Bloecker 1995; Habing & Olofsson 2003). In the lower metallicity environments of the LMC and SMC, it is expected that the wind speed in O-AGB stars is smaller compared to their Galactic counterparts (Marshall et al. 2004). We adopt a constant outflow velocity for the dust of $v_{\rm exp} = 10$ km s^{-1} for all the Magellanic Cloud objects (Wood et al. 1992; van Loon et al. 2001). For the assumptions adopted in this paper, the mass-loss rate is linearly related to the actual individual expansion velocity via $\dot{M} \propto v_{\rm exp}/(10\,{\rm km\,s^{-1}})$.

Total mass-loss rates are varied from 10^{-10} to 10^{-5} M$_\odot$ yr^{-1} and the dust-to-gas ratio is taken to be $\Psi = 0.005$ which is typically used for O-AGB stars in the LMC (Groenewegen 2006; Sargent et al. 2011; Srinivasan et al. 2011).

This enables us to encompass a large range of spectral morphologies, from 'naked' (dust-free) stars to stars heavily enshrouded by circumstellar dust with a large IR excess ([3.8] − [8] > 0.8). Our model grid extends to a colour of [3.8] − [8] = 2.4 which covers 95 per cent of the confirmed O-rich AGB stars in the LMC. Extreme O-rich stars that are redder than this limit have mass-loss rates greater than 10^{-5} M$_\odot$ yr^{-1} (Groenewegen et al. 2009).

However, caution must be taken when comparing models with low dust-production rates ($\dot{D}$) to observations, as it is very difficult to differentiate stellar photospheres from sources with very low-contrast dust features below $\dot{D} \approx 10^{-11}$ M$_\odot$ yr^{-1} (Riebel et al. 2012), since the dust-emission contrast (DEC) is proportional to the dust-production rate.

For all our models, a distance of 49.97 kpc to the LMC is assumed (Pietrzyński et al. 2013).

2.1.3 *Dust grain properties*

The circumstellar envelopes of O-AGB stars are mineralogically complex. For stars with low mass-loss rates ($\dot{M} < 10^{-7}$M$_\odot$ yr^{-1}), simple metal oxides are the most abundant species (Cami 2002; Posch et al. 2002); at greater mass-loss rates, silicates (in both amorphous and crystalline form) become the dominant dust component. Metallic iron grains are thought to also contribute to the IR emission around oxygen-rich AGB stars (Kemper et al. 2002; Verhoelst et al. 2009; McDonald et al. 2010), and iron may be incorporated in other dust grains, for example in amorphous silicates (Gail & Sedlmayr 1999).

The chemical composition of amorphous silicate grains is not well known, and previous studies of oxygen-rich AGB stars have considered a wide range of dust compositions with varying success. In Fig. 1, we compare five sets of 'astronomical silicates' and two dust compositions obtained from laboratory measurements to *Spitzer* infrared spectrograph (IRS) observations of O-rich AGB stars in the LMC. The astronomical silicates we consider are the oxygen-deficient (Opoor) and oxygen-rich (Orich) silicates from Ossenkopf, Henning & Mathis (1992), the 'warm' and 'cool' silicates from Suh (1999), and the Draine & Lee (1984) astronomical silicates derived from interstellar medium lines of sight. For the laboratory measured dust species, we consider the amorphous olivine refractory indices from Jäger et al. (2003) and Dorschner et al. (1995).

We find that the pure amorphous olivine from Dorschner et al. (1995) best reproduce the position and relative strengths of the 10 and 20 μm features in the IR spectrum of O-rich AGB stars in the LMC. We assume that the stoichiometric composition of the amorphous silicate dust grains is not dependent on the mass-loss rate of the AGB star.

To increase the opacity in the near-IR region, we also include metallic iron, using laboratory data from Ordal et al. (1988). We adopt a metallic iron abundance of 4 per cent by mass with respect to the amorphous silicates, following Kemper et al. (2002) and de Vries et al. (2010).

For the refractive indices of amorphous alumina dust, we use the optical constants for porous alumina grains measured by Begemann et al. (1997), which are extended to shorter wavelengths ($\lambda < 7.8$ μm) by concatenation with optical constants from Koike et al. (1995).

For all dust species modelled, we adopt a standard Mathis–Rumpl–Nordsieck (MRN) grain-size distribution (Mathis, Rumpl & Nordsieck 1977), given by $N(a) \propto a^{-q}$, with $q = 3.5$, for a grain-size range of $a = 0.01$–1 μm. To calculate the absorption and scattering coefficients of the dust grains from the complex refractive indices measured in the lab, an assumption about the grain shape distribution needs to be made; we adopt a continuous distribution of ellipsoids (CDE) for the particle shape (Bohren & Huffman 1983). This is preferred over homogeneous spherical grains as regularly shaped particles introduce resonance effects resulting in unrealistic feature shapes (Min, Hovenier & de Koter 2003).

The alumina abundance was varied in increments of 5 per cent for 0–40 per cent and increased in steps of 10 per cent for 40–100 per cent. Spectra with different alumina abundances are shown in Fig. 2; there is a clear change in the shape and strength of the 10-μm feature as the alumina abundance is increased.

3 MODEL RESULTS

From our models, we compute expected flux densities for the broad-band filters of 2MASS, *Spitzer*, *WISE* and *AKARI* by convolving the MODUST spectral output with the relative spectral response curves.[1]

[1] Filtercurves were obtained from the official websites: http://www.ipac.caltech.edu/2mass/releases/allsky/doc/sec6_4a.html; http://ssc.spitzer.caltech.edu/irac/spectral_response.html; http://ssc.spitzer.caltech.edu/mips/spectral_response.html; http://www.astro.ucla.edu/∼wright/WISE/passbands.html and http://www.ir.isas.jaxa.jp/ASTRO-F/Observation/RSRF/IRC_FAD/index.html

Downloaded from http://mnras.oxfordjournals.org/ at Cornell University Library on April 16, 2016

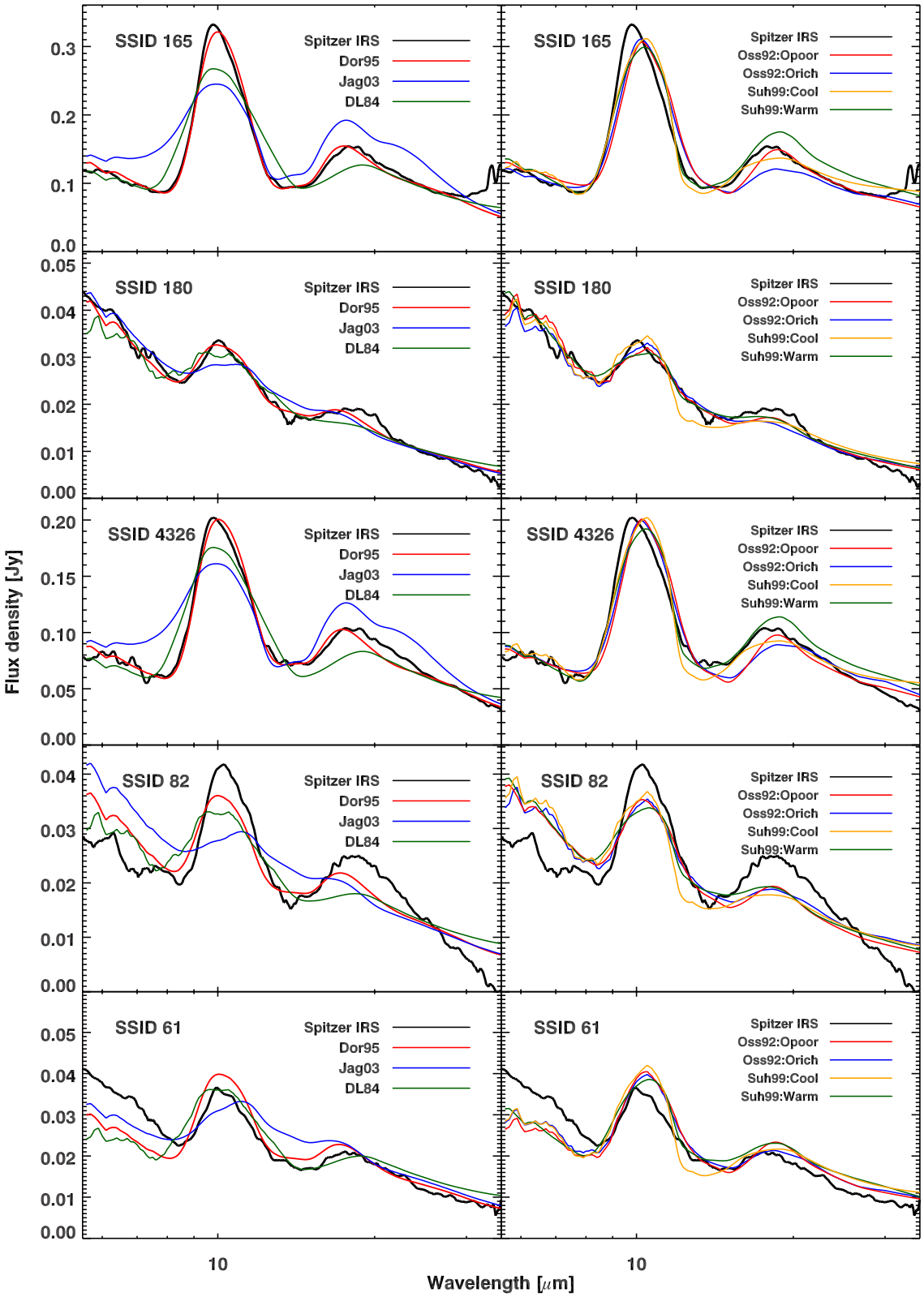

Figure 1. Comparison of astronomical and laboratory silicates to *Spitzer* IRS observations of O-rich AGB stars in the LMC. The optical constants derived by Dorschner et al. (1995) provide the best overall fit to the spectra.

Downloaded from http://mnras.oxfordjournals.org/ at Cornell University Library on April 16, 2016

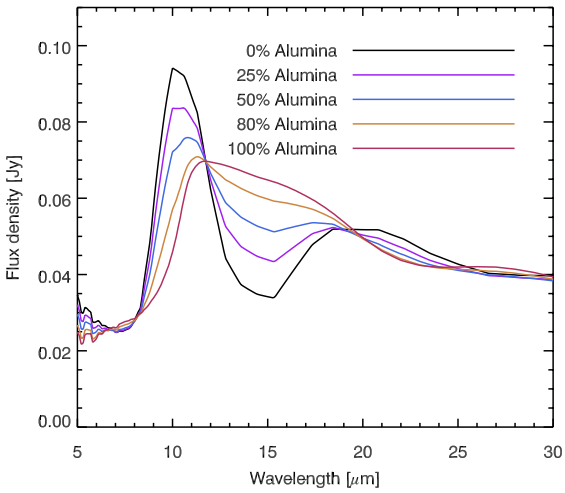

Figure 2. Five spectra with different alumina abundances are shown, for $\dot{M} = 7.5 \times 10^{-7}\,\mathrm{M}_{\odot}\,\mathrm{yr}^{-1}$. All other model parameters are constant.

The calculated fluxes are further converted into Vega magnitudes, which can be directly compared to catalogue values.

3.1 Colour–colour diagrams

In this section, we show examples of the colour–colour space occupied by our grid of models and compare our synthesized photometry to observations of evolved stars. Since our models are created for dusty O-rich AGB stars, we focus on mid-IR colours, where molecular and dust spectral features cause distinct photometric signatures and the central star's effective stellar temperature has little influence on the flux.

Mid-IR CCD for the model grid are presented in Figs 3–5. For comparison, we also include LMC point sources from the SAGE-Spec survey, which were identified as O-rich AGB stars and red supergiants (RSGs) using *Spitzer* IRS spectra and ancillary photometry (Kemper et al. 2010; Woods et al. 2011; Jones et al. 2012). These were cross-identified with the *AKARI* LMC point source catalogue (Ita et al. 2008; Kato et al. 2012) and the *WISE* all-sky catalogue (Wright et al. 2010).

In general, our models are consistent with the range of observed colours for oxygen-rich stars in the CCD considered here, especially when the contributions from circumstellar dust becomes significant in describing the observed photometry. However, the resolution of the grid before dust production begins is limited to narrow columns in colour–colour space (Fig. 4), corresponding to sets of models with low optical depths derived from the three input stellar photospheres. The sparse grid coverage for the dust-free sources reflects the compromise between the accuracy of the model fit and the required computational time, with emphasis placed on the fine sampling of model AGB stars with apparent dust excesses.

The Infrared Array Camera (IRAC) [5.8]−[8.0] versus [3.6]−[4.5] CCD, shown in the left-hand panel of Fig. 3, traces the photospheric temperature of the central star and continuum emission from the circumstellar dust shell. At these wavelengths, O-rich dust has no distinguishable signatures, unless it contains a significant fraction of iron or has a strong 10-μm silicate feature, both of which affect the 8-μm flux. The IRAC colours are insufficient to distinguish between carbon-rich AGB stars, oxygen-rich AGB stars and RSGs, as such there is a significant overlap between the carbon-rich dust sources and our oxygen-rich models. The largest discrepancy between our model grid and observations is for sources that lie in the largely dustless region below [5.8]−[8.0] < 0.6 mag. These sources have little circumstellar excess and may be better represented by photospheres with a larger range of stellar effective temperatures, metallicity and surface gravity. With the onset of mass-loss, the dust emission increases and the model colours provide better coverage of the observed data. For sources with a dust excess, discrepancies between the models and observations may be accounted for by altering the metallic iron abundance, which influences the [3.6]−[4.5] colour in O-rich stars.

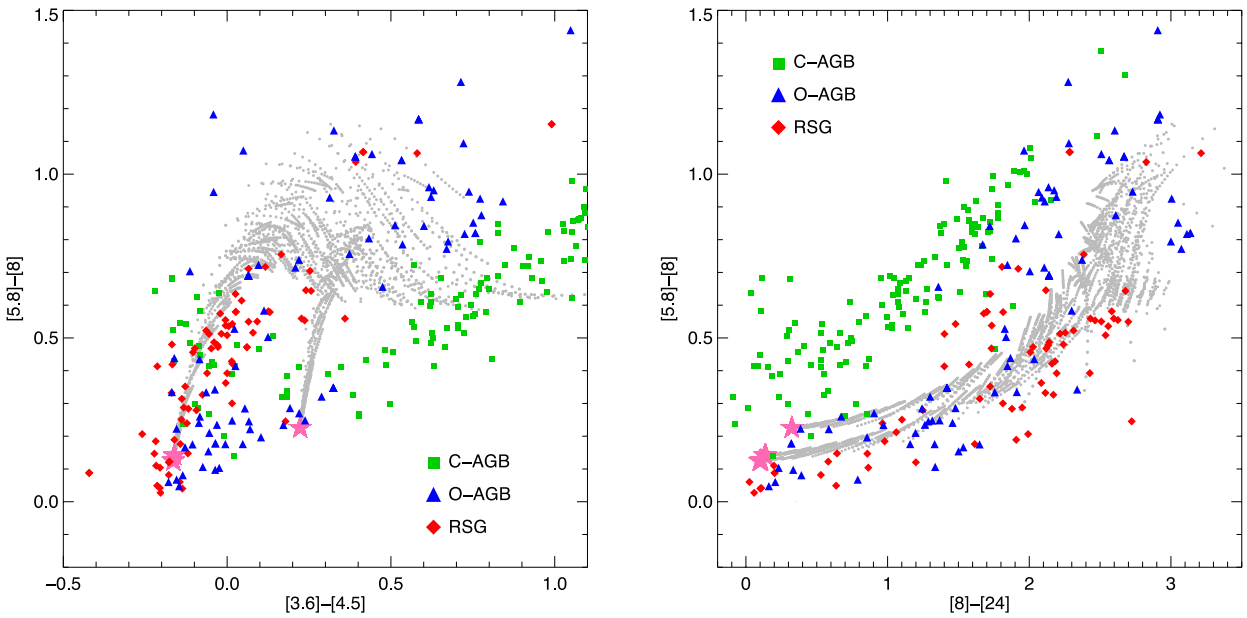

Figure 3. *Spitzer* IRAC/MIPS CCD for two combinations of colours. The small, grey dots denote the models from our O-rich grid. Also shown are the Fluks et al. (1994) photospheres (pink stars) used to generate the grid. To illustrate the model grid coverage, the evolved sources in the SAGE-Spec sample are overlaid: O-rich AGB stars are represented by blue triangles, RSGs by red diamonds and C-rich AGB stars by green squares.

Downloaded from http://mnras.oxfordjournals.org/ at Cornell University Library on April 16, 2016

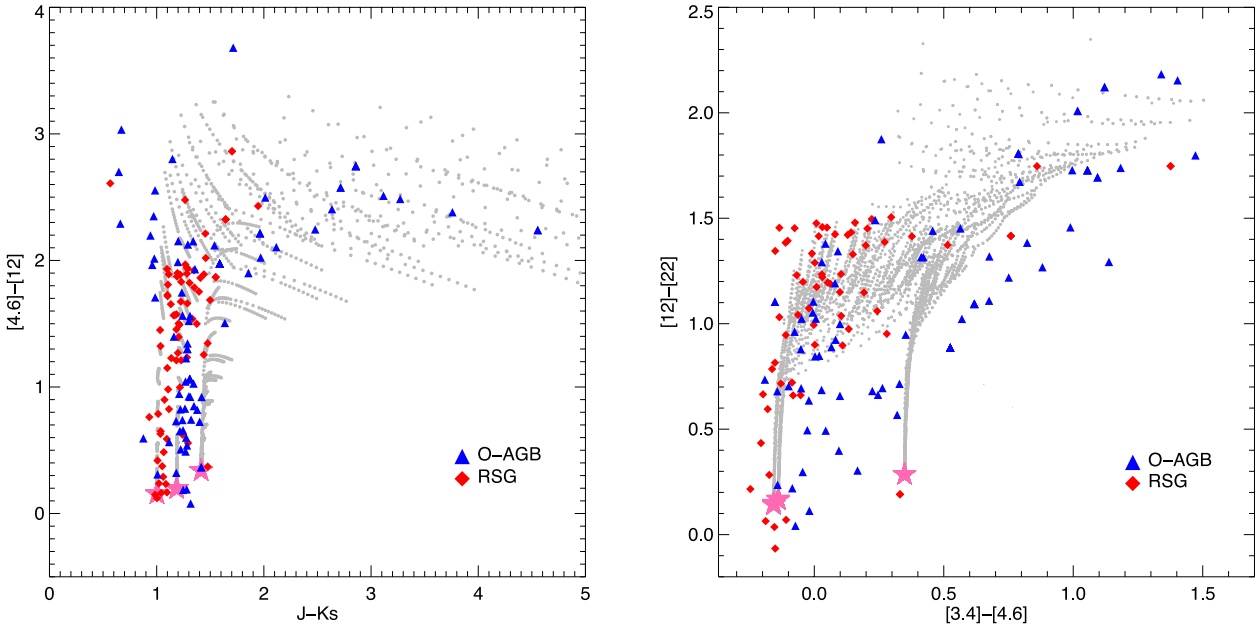

Figure 4. 2MASS–*WISE* $J - K_s$ versus [4.6] − [12] CCD (left) and *WISE* [12] − [22] versus [3.4] − [4.6] CCD (right) of the known O-AGB and RSG stars in the SAGE-Spec sample. The symbols are as in Fig. 3.

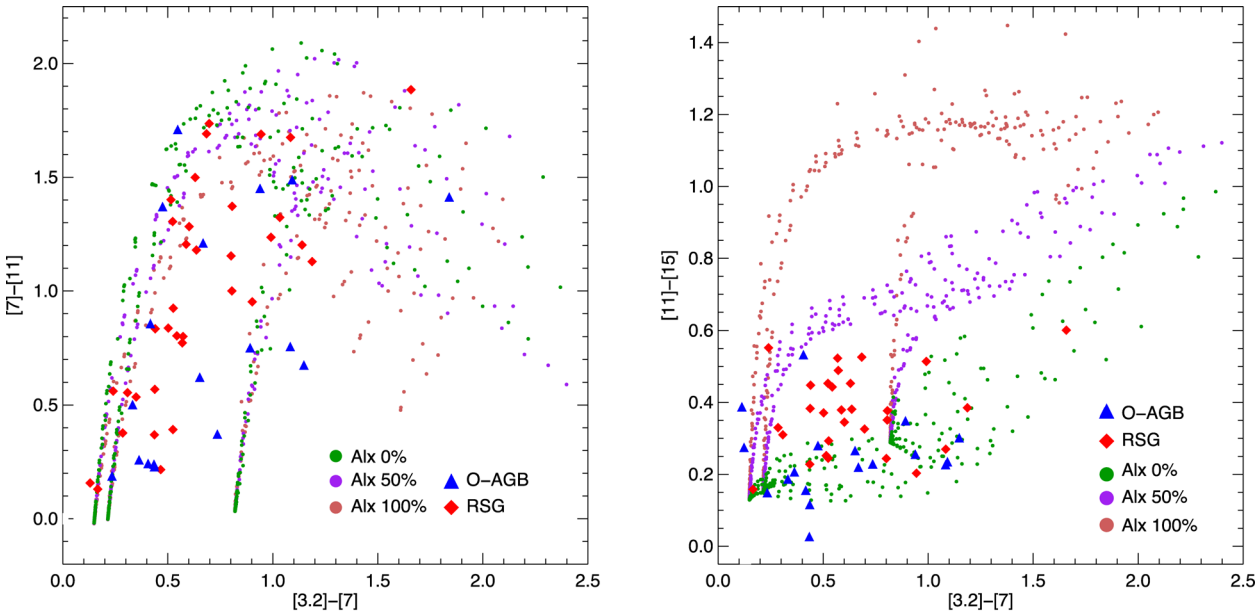

Figure 5. *AKARI* CCD for two combinations of colours. Models with pure amorphous silicates (green), pure alumina (brown) and an equal blend between alumina and silicates (purple) are highlighted. All other symbols are as in Fig. 3.

Moving to longer wavelengths, the [5.8]−[8] versus [8]−[24] CCD (Fig. 3; right-hand panel) is an effective tracer of stars with significant amounts of circumstellar dust. It is often used to distinguish oxygen-rich from carbon-rich stars as there is little overlap between the populations (Kastner et al. 2008; Boyer et al. 2012). Our models on the whole show a considerable overlap with the colours of the O-rich AGB stars from SAGE-Spec sample but are well separated from the region occupied by the C-rich AGB stars.

The left-hand panel in Fig. 4 shows a CCD incorporating both near- and mid-IR data. This essentially compares the model photospheres via the $J - K_s$ colour to the dust excess, traced by the *WISE* [4.6]−[12] colour. In the diagram the different stellar types are reasonably well separated (due to differences between the stars effective temperature), until the stars become heavily dust enshrouded at [4.6]−[12] > 1.6. The observed RSGs, with bluer ($J - K_s$) colours, are generally traced by models with an M1 photosphere, while the O-AGB stars that have slightly redder $J - K_s$ colours are represented by the cooler M5 and M9 photospheres. The models reproduce the range of observed colours quite well, except for sources which lie off to the left of the model grid. This discrepancy is most likely due to an enhanced scattering by dust in an asymmetric shell or due to pulsations which can significantly affect the near-IR flux of AGB stars (Whitelock et al. 2003). For Mira variable stars, pulsation amplitudes are typically in the region of 6–8 mag in *V* and are usually

Downloaded from http://mnras.oxfordjournals.org/ at Cornell University Library on April 16, 2016

less than 2.5 mag in *K*. RSG are typically less variable than AGB stars; this class of objects has a lower fraction of sources which diverge from the model grid, in this case, scattering of light in an asymmetric dust shell may be important.

The *WISE* [12]−[22] versus [3.4]−[4.6] CCD shown in the right-hand panel of Fig. 4 has a similar model coverage to the *Spitzer* [5.8]−[8.0] versus [3.6]−[4.5] CCD. The *WISE* [3.4]−[4.6] colour is comparable to the *Spitzer* IRAC [3.6]−[4.5] colour and is a good indicator of the emission from the warmest regions of the dust shell, while the 12- and 22-μm filters measure the emission from the silicate features at 10 and 20 μm, and thus this colour is a good tracer of oxygen-rich dust. As before a number of the O-rich AGB and RSG stars which contain little or no dust around them are not covered by the model grid. Additionally, some sources with [3.4]−[4.6] > 0.5 mag and [12]−[22] < 1.5 mag fall outside the region covered by our model grid; these sources may be better represented by models with a higher percentage of metallic iron grains in the circumstellar shell, which would increase the [3.4]−[4.6] colour.

Fig. 5 shows two-colour diagrams using *AKARI* colours of [7]−[11] versus [3.2]−[7] and [11]−[15] versus [3.2]−[7]. The models with pure amorphous silicates, pure alumina and an equal blend between alumina and silicates are highlighted. While there is considerable degeneracy in the [7]−[11] colour, which measures the 10-μm feature irrespective of the Al_2O_3 content; the [11]−[15] colour provides a measurement of the change in strength/shape of the 10-μm dust feature. This diagram separates the different dust types well, in sources with a reasonable dust excess. It can therefore be used as a diagnostic to derive the fractional abundance of alumina (Alx). The sources in the SAGE-Spec sample occupy a region in colour–colour space corresponding to an alumina fraction of less than 50 per cent (we return to this in Section 4).

3.1.1 *Comparison to the GRAMS model grid*

In a recent similar study, Sargent et al. (2010) and Srinivasan et al. (2011) developed the GRAMS to reproduce the range of observed IR colours of LMC RSG and AGB stars, and to measure their luminosities and dust-production rates. The GRAMS grid consists of models for oxygen-rich as well as carbonaceous chemistries; the O-rich models (Sargent et al. 2010) consist of oxygen-deficient silicate grains from Ossenkopf et al. (1992), while the carbon-star dust (Srinivasan et al. 2011) is composed of a mixture of amorphous carbon and silicon carbide, the latter making up 10 per cent of the mass. The authors used the 2DUST code (Ueta & Meixner 2003) to solve the radiative transfer problem for a dust shell of given inner and outer radius, and optical depth around a central star that was represented by a model photosphere. They chose the range of input parameters (inner radii, optical depths) to cover the expected and observed values for LMC evolved stars.

We compare our model output to the O-rich GRAMS models in Fig. 6. Overall, there is good agreement between the sets of oxygen-rich models, particularly in the IRAC bands at shorter wavelengths ($\lambda < 8$ μm). In the near-IR, the GRAMS grid agrees better with the bluer stellar sequences where stellar temperature has a greater influence on the colour. Although both sets of model grids cover a similar range in stellar effective temperatures, the 14 PHOENIX stellar photosphere models (Kučinskas et al. 2005, 2006) used in the O-rich GRAMS grid has a finer effective temperature resolution. The metallicities of the photospheres are also different; however, for dusty stars this has a minimal effect on the broad-band photometry and colour. In the mid-IR, our models span a wider range of colour space due in part to the inclusion of alumina and the choice of optical constants for the amorphous silicates. It should also be noted that two models that overlap in colour–colour space may not necessarily have the exactly same input parameters.

3.2 SE index

The silicate emission (SE) index is a spectral classification system developed by Sloan & Price (1995, 1998) to measure the variation in the shape/strength of the emission feature at about 8–12 μm in optically thin oxygen-rich AGB stars. The observed spectra are divided into eight categories (SE 1–8) based on the ratios of

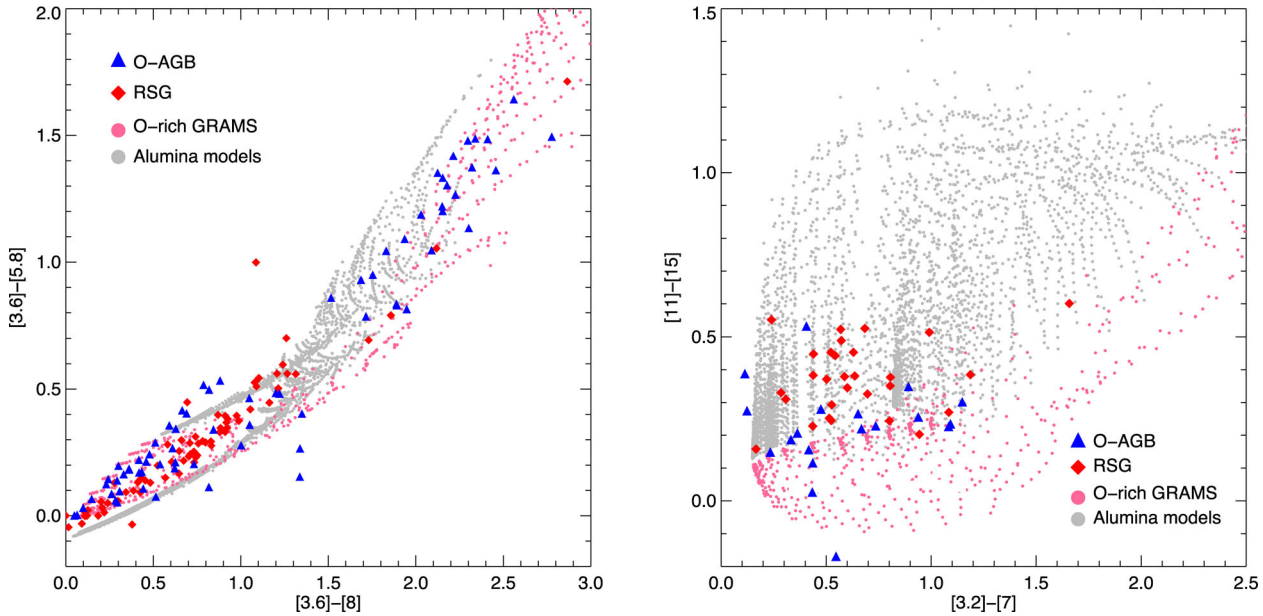

Figure 6. Comparison of the coverage of the model grid described in this work with the oxygen-rich GRAMS models (pink points).

Downloaded from http://mnras.oxfordjournals.org/ at Cornell University Library on April 16, 2016

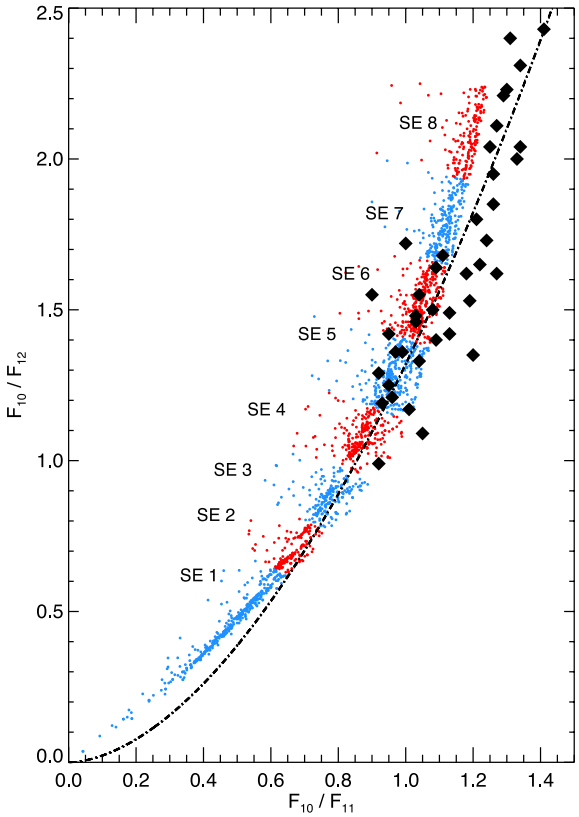

Figure 7. The silicate dust sequence power law, $F_{10}/F_{12} = 1.32(F_{10}/F_{11})^{1.77}$ (dotted black line; from Sloan & Price 1995), and the flux ratios for the individual models. For comparison, the filled black diamonds show the flux ratios of LMC O-AGB sources.

narrow-band fluxes at 10, 11 and 12 μm (F_{10}, F_{11} and F_{12}). These classes are designed to reflect the progression from the broad oxygen-rich dust emission features with little structure (SE 1–3) to the classic narrow 9.7-μm silicate features (SE 7–8).

The change in spectral features represents the dust formation process along the AGB, which depends strongly on $\dot{M}$ (Dijkstra et al. 2005). We would therefore expect the SE index to reflect the mass-loss rate, the chemical composition of the dust grains (i.e. the relative abundances of silicates and amorphous alumina) and variations in the temperature of the dust shell (Ivezic & Elitzur 1995; Hron, Aringer & Kerschbaum 1997; Egan, Van Dyk & Price 2001).

To investigate the parameter space covered by each SE class, we apply the spectral classification procedure of Sloan et al. (2003) to each optically thin model in our grid. To isolate the dust emission, we subtract the appropriate stellar photosphere used in constructing the model. Each model's dust excess was quantified via the DEC, defined as the ratio of dust emission to stellar emission between 7.67 and 14.03 μm (Sloan et al. 2008). In keeping with observations, and to prevent any overinterpretation of models with no significant dust excess, we do not ascribe an SE class to models with DEC $\leq$ 0.10. This corresponds to all models with a mass-loss rate below $\dot{M} \sim 3 \times 10^{-9}\,\mathrm{M}_{\odot}\,\mathrm{yr}^{-1}$.

Fig. 7 shows the F_{10}/F_{12} versus F_{10}/F_{11} model flux ratios and the empirically derived silicate dust sequence power law: $F_{10}/F_{12} = 1.32(F_{10}/F_{11})^{1.77}$ (Sloan & Price 1995), which forms the basis for the SE index classification. Our models reproduce each of the eight SE indices along the silicate dust sequence; SE classes one and eight contain the largest numbers of models, with

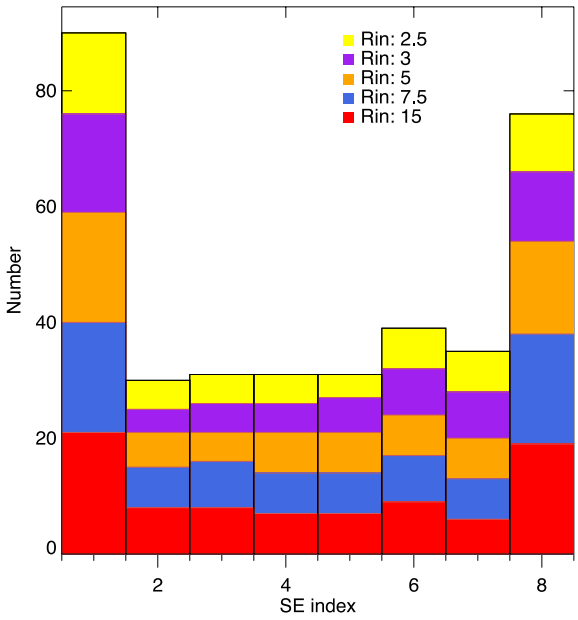

Figure 8. Distribution of the model grid SE index. Each colour represents a dust-shell inner radius explored by the grid for models with an M9 stellar photosphere. The even distribution between R_{in} models suggests that the SE index is independent of the dust temperature.

the remainder equally distributed across SE indices 2–7. This due to sources falling outside the SE 1–8 range being classified as either SE1 or SE8.

There is a slight deviation from the silicate dust sequence power law at SE8. Observationally, sources in the Milky Way tend to occupy a region to the right of the silicate dust sequence for SE8, while stars from low-metallicity Galactic globular clusters populate a region to the left of the sequence (Sloan et al. 2008, 2010). At the other end of the SE sequence, we suspect that the curvature arises due to the models in our grid with high mass-loss rates combined with a high fractional abundance of alumina (Alx).

The distribution of SE classes for our model grid is shown in Fig. 8. Segregating the models according to the inner radius of the dust shell has no significant effect upon the SE index distribution, which suggests that the SE index is independent of the dust temperature. This is not surprising as the SE index is calculated using flux ratios across the 10-μm feature of a given temperature, effectively eliminating the grain temperature parameter. Since we have isolated the dust emission, the SE index is also independent of the spectral type and the effective temperature of the central star.

Fig. 9 illustrates the range in mass-loss rate and alumina abundance covered by each SE class. Increasing the density of the shell leads to models moving upwards and to the right along the SE sequence; however, changes in position are generally too small to move a model to a higher SE class. For models dominated by either pure alumina or silicates, the shell density may have a greater influence as it determines when the emission from the dust shell becomes significant compared to that of the stellar photosphere.

The composition of the dust has a more substantial effect on the SE index than the mass-loss rate. For a given mass-loss rate, a blend of alumina and silicates can reproduce the full silicate dust sequence. SE classes 1–3 are successfully reproduced by shells dominated by alumina dust (Alx $\gtrsim$ 70 per cent), while classes SE 6–8 are populated by models dominated by amorphous silicates (Alx $\lesssim$ 50 per cent).

Downloaded from http://mnras.oxfordjournals.org/ at Cornell University Library on April 16, 2016

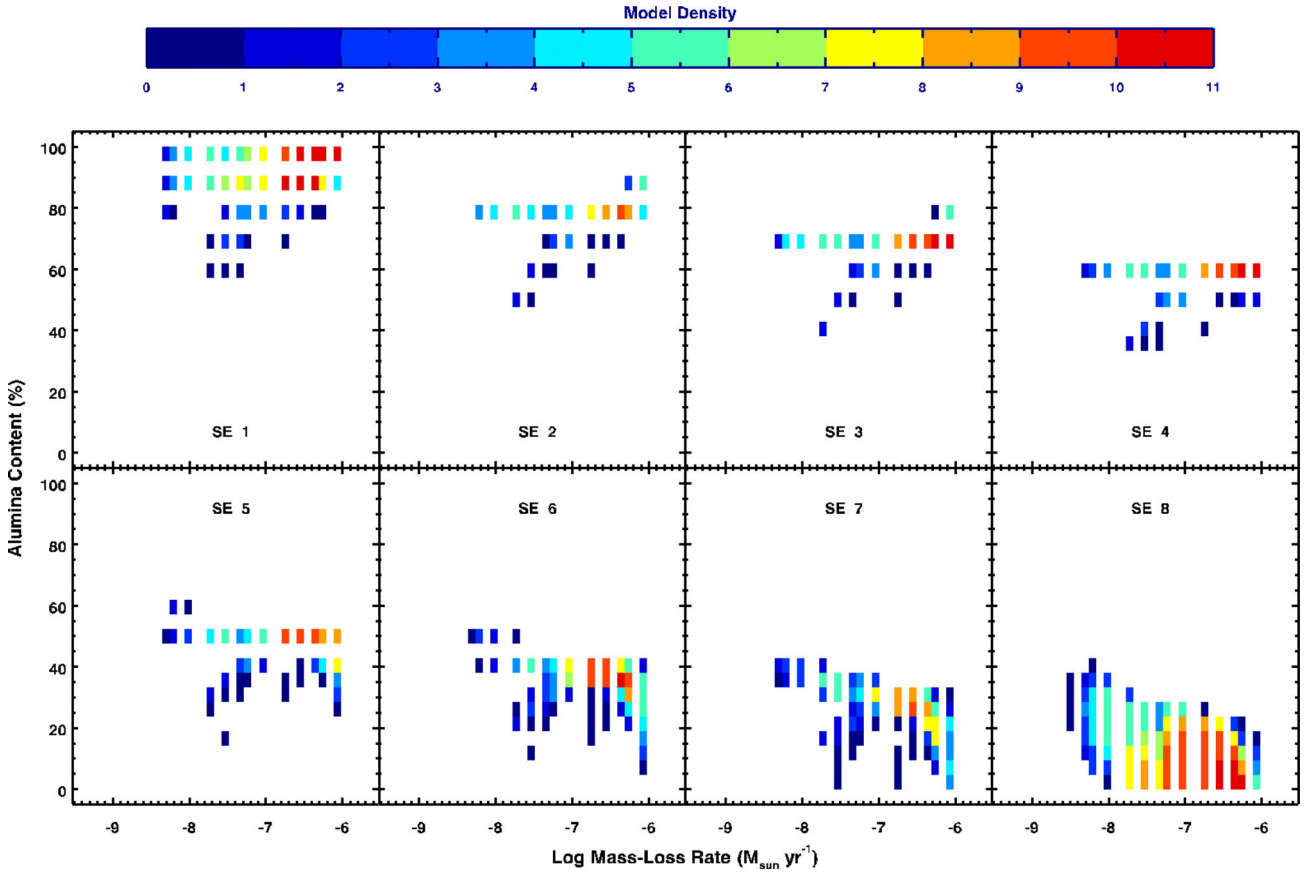

Figure 9. The relationship between the alumina content and total mass-loss rate for the models in our grid with a dust excess, separated according to the SE index.

The distribution of the O-rich AGB stars in the LMC with SE index is shown in Fig. 10. This suggests that the dust in the LMC is primarily silicate-rich, whilst alumina is largely absent, in agreement with the alumina dust abundances derived from *AKARI* photometric colours in Fig. 5. However, our spectroscopic sample only includes relatively bright AGB stars in the LMC, which have sufficient signal-to-noise ratio in their IRS spectra to quantify the dust excess. Thus, the lack of sources with a low SE index could be due to an observational bias.

4 MEASURING THE ALUMINA FRACTION

To estimate the alumina content of AGB stars in the LMC, we apply our model grid to the sample of 54 O-rich AGB stars described by Jones et al. (2012) taken from the *Spitzer* SAGE-Spec sample of Kemper et al. (2010) and the archival IRS spectra in the LMC. As alumina has not been observed in optically thick AGB envelopes, we excluded the sources where the 10-μm feature is in self-absorption from our analysis. Also excluded are sources that essentially appear as stellar photospheres with no significant IR excess due to dust emission but have been classified as AGB stars due to molecular absorption features and photometric variability. From this, we are left with 37 sources.

To model the AGB stars, we have scaled the IRS spectrum to match the IRAC 5.8- and Multiband Imaging Photometer of *spitzer* (MIPS) 24-μm fluxes to enable an accurate comparison to photometry. For each star, we fitted the models to the observed broad-band JHK_s, IRAC and MIPS 24-μm photometric data, and the flux measured over set wavelength intervals (line segments) from the spectra. This allows us to achieve a good fit to both the spectral energy distribution (SED) and the observed spectrum. The line segments have continuous wavelength coverage over the full *Spitzer* spectral range and each of the nine bands cover equal widths in logarithmic

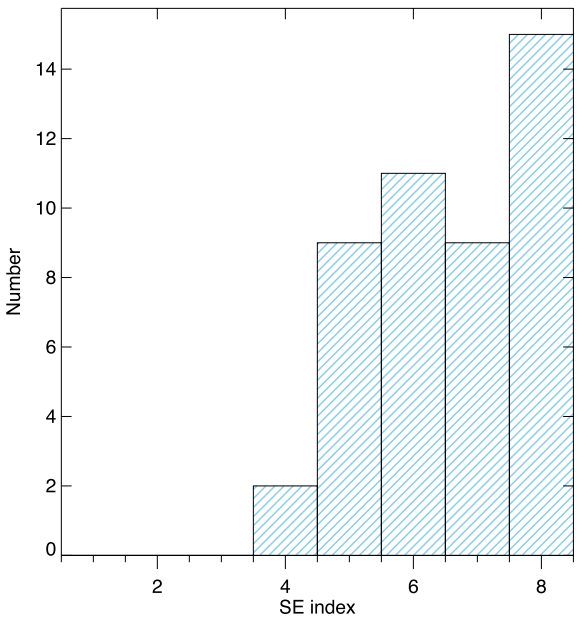

Figure 10. Distribution of the O-rich AGB stars in the LMC with SE index.

Downloaded from http://mnras.oxfordjournals.org/ at Cornell University Library on April 16, 2016

wavelength. This gives more weight to shorter wavelengths where the dust grains emit most of their flux and where the dust optical constants provide greater constraints to the observed emission feature profiles. An additional six narrow bands (0.38 μm wide) over the 8–13-μm interval provide detailed measurements of the 10-μm feature. These 15 bands measure the spectral flux and place a strong constraint on the individual dust species present in the IR spectrum. This is essential, as fits based only on the photometric data points poorly constrain the relative strengths of the dust features.

Comparisons between the models and the data were made with an automated fitting routine, and the best fit was selected based on a chi-square (χ^2_ν) minimization technique. The quality of the best-fitting model was defined by

$$\chi^2_\nu = \frac{1}{N-p}\sum_i \frac{(f_{\mathrm{obs}_i} - f_{m_i})^2}{\sigma_i^2}, \quad (2)$$

where f_{obs_i} and f_{m_i} are the observed and model flux in the ith band with error bar σ_i, N is the total number of data points being fitted and p is the number of free parameters in the model. Uncertainties in the photometric data were modified to account for variability across a pulsation cycle (see Jones et al. 2012; Riebel et al. 2012), and uncertainties in the spectroscopic data were inflated by a factor of 5 (see Groenewegen et al. 2009).

Our models are computed for a single luminosity, therefore they must be scaled to match the luminosity of the source in question before performing the χ^2 fitting. The luminosity (L) of the source can be computed from this scaling factor (η) via $\eta = (L/7000\,\mathrm{L}_\odot)(d/49.97\,\mathrm{kpc})^2$, where the distance ($d$) is assumed to be 49.97 kpc for the LMC. As the luminosity is scaled, so too must the wind parameters be scaled appropriately. Following equation (2) of Groenewegen (2006), the stellar radius and the mass-loss rate must scale by the factor $\sqrt{\eta}$. The other model parameters and outputs are independent of this scaling.

Several models may provide a good fit to a source (defined arbitrarily by $\chi^2 - \chi^2_{\mathrm{min}} < 3$). To gauge the range a parameter could vary for a given source, we calculate its median absolute deviation; this is more resilient to outliers than the standard deviation and thus provides a more robust estimator of the uncertainty. The SEDs and spectra for all the O-AGB stars in our sample (identified by the SAGE-Spec designation; SSID) along with the best-fitting model for each source are shown in Fig. 11. To estimate a threshold value in the alumina abundance where its inclusion truly improves the fit, we also calculate the best fit using models with a fixed oxygen-rich dust composition without an alumina component. We find that the adoption of amorphous alumina grains in the model significantly improves the fit when its abundance is greater than 15 per cent. The modelling results are summarized in Table 2.

Eight stars in our spectroscopic sample have also been observed with *AKARI* at 3.2, 7, 11, 15 and 24 μm. This provides additional photometric coverage in the mid-IR spectral region useful for distinguishing the dust composition. For these sources, we also determine the best-fitting model using only the photometric data from the *Spitzer* SAGE and *AKARI* LMC point source catalogues, to see how the model parameters (particularly the alumina abundance) are affected by the exclusion of the spectrum. The best fit obtained using only the photometry is shown in Fig. 12, and the results summarized in Table 3.

All the O-AGB stars in our sample exhibit significant dust emission. Although the 10-μm feature is apparent in each spectrum, it exhibits a considerable variation in shape and there is a broad variety in the other spectral features between individual stars. At this stage, it is worth remembering that the model grid is intended to provide an initial estimate to the fitting parameters and that each best model fit can be optimized by fine-tuning the model values on an individual basis.

In general, the fitting of the models to the spectra plus the SED is of a high quality for an automated routine and the model grid is very successful at reproducing the observed shape of the 10-μm feature. The model fits to the SED without the additional information from the spectra also reproduce the observations; however, the constraints on the model parameters, in particularly the alumina abundance, are less robust. We find that the combined SAGE and *AKARI* photometric data allows us to identify stars with a significant alumina component in the majority of sources; however, for stars with a very low contrast 10-μm feature (e.g. SSID 4449), spectroscopic information is still required.

At longer wavelengths ($\lambda > 16$ μm), the models are less successful in reproducing the broad emission feature at 18 μm and the slope of the continuum in the observed spectra. This discrepancy is due in part to the choice of optical constants; in laboratory silicates, the 18-μm emission feature peaks at too short a wavelength compared to observations and its strength is often too strong with respect to the observed 10-μm feature. Conversely, astronomical silicates provide a better fit to the 20-μm region; however, the shape is broader than observed and they overpredict the flux in the 10-μm region and cannot reproduce its shape and position. More complicated situations are not considered in the model such as different spatial density distributions of the dust; deviations from spherical symmetry; or a steeper density profile, which may cause deviations between the model and the observations at longer wavelengths.

In some stars (for example, SSID 4329), there is a small discrepancy between the models and the spectra in the 4–8-μm wavelength region. The inclusion of iron grains is necessary to reproduce the general slope of the SED and explain excess emission in the spectra up to 8 μm, as laboratory silicates provide too little opacity in the near-IR (Kemper et al. 2002; Verhoelst et al. 2009; McDonald et al. 2010). Other proposed sources of this excess continuum emission include amorphous carbon (Demyk et al. 2000) or micron-sized O-rich dust grains (Höfner 2008; Norris et al. 2012). In these cases, the metallic iron abundances may need to be increased in order to reproduce the observed profiles. In this study, we use an iron abundance of 4 per cent with respect to the amorphous silicates; however, Groenewegen et al. (2009) find that a value of 5 per cent provides the best fit.

While the adoption of iron grains has generally worked well, in one instance (SSID 182) its inclusion proves detrimental to the fit. Fig. 13 shows the best-fitting models to SSID 182. The total mass-loss rate for both models was $\sim 1.4 \times 10^{-7}\,\mathrm{M}_\odot\,\mathrm{yr}^{-1}$ and the alumina mass fraction ∼15 per cent. The inclusion of metallic iron has a greater influence on the dust-shell inner radius, which determines the temperature of the hottest dust.

In our modelling, we only use three dust components: amorphous silicates, amorphous alumina and metallic iron; this grain mixture fits the observed spectra well. Other dust components that may be present but are not taken into account include crystalline silicates, gehlenite ($Ca_2Al_2SiO_7$) and spinel ($MgAl_2O_4$). Three spectra (SSID 22, 182 and 419) have strong crystalline silicate complexes near 23, 28 and 33 μm, which will contribute some flux to the underlying continuum. A more detailed description of the crystalline silicate features in the present sample can be found in Jones et al. (2012).

Previously, calcium–aluminium-rich silicates, such as gehlenite ($Ca_2Al_2SiO_7$), have been detected in significant amounts (25–50 per cent) around O-rich evolved stars with low mass-loss rates

Downloaded from http://mnras.oxfordjournals.org/ at Cornell University Library on April 16, 2016

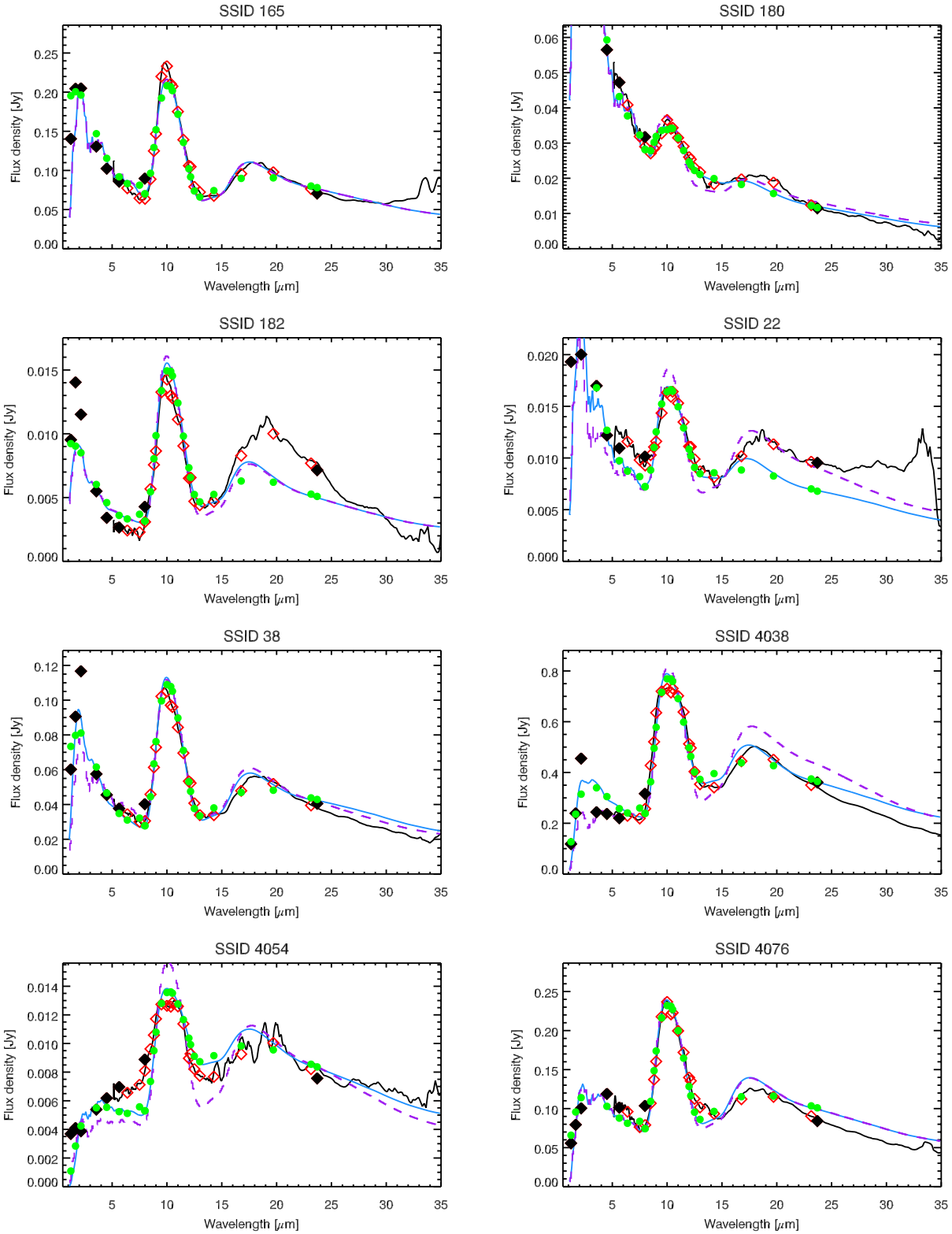

Figure 11. The observed *Spitzer* spectra of O-rich AGB stars (black) and the corresponding best-fitting model (blue). The photometric points are shown as black diamonds, the flux from the spectral segments as red diamonds and the synthetic flux from the models are green circles. The least-squares fit is performed by matching the green model points to the red/black data points. The black and blue lines are only shown for illustration purposes. For comparison, the best-fitting model without an alumina component is indicated by a dashed purple line.

Downloaded from http://mnras.oxfordjournals.org/ at Cornell University Library on April 16, 2016

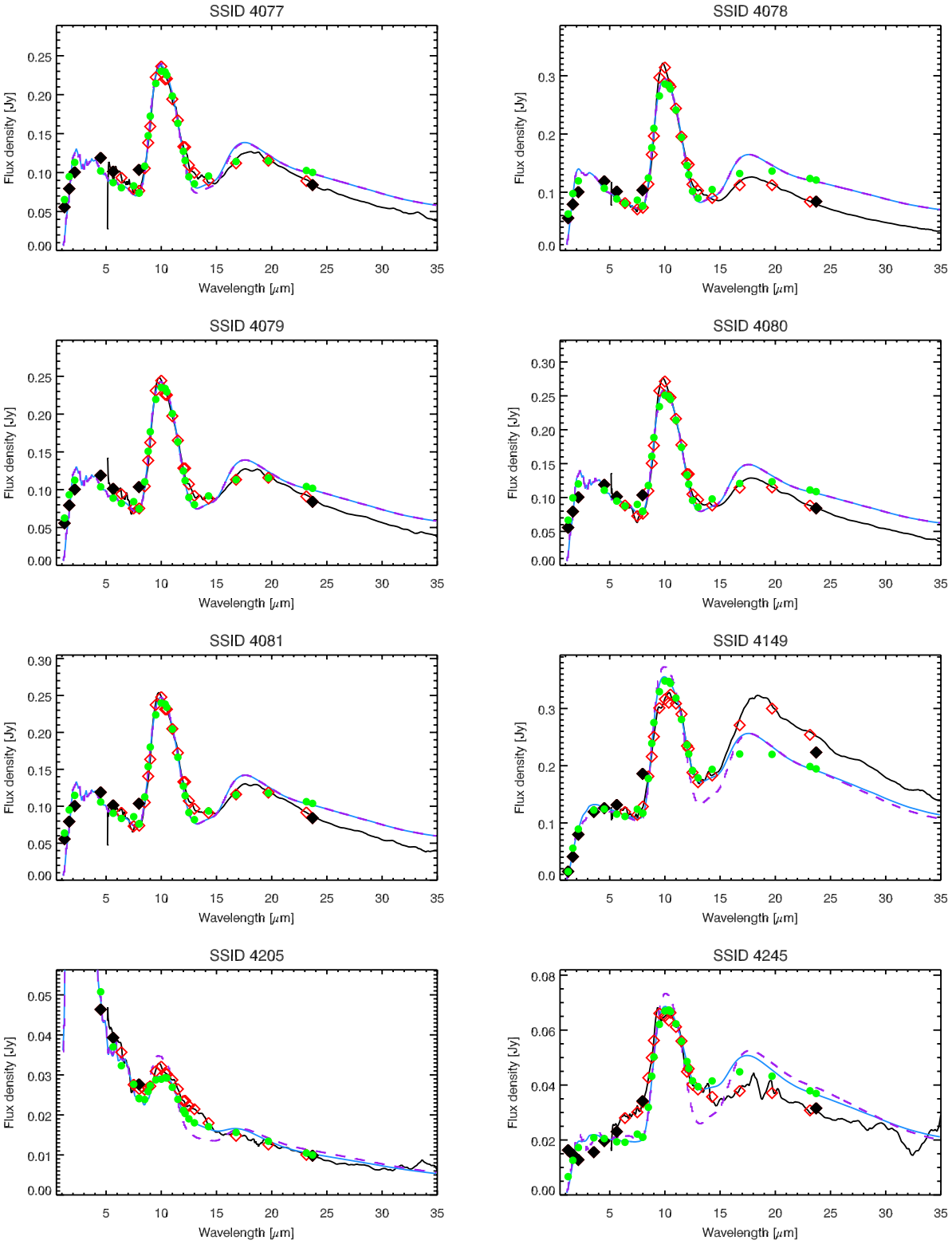

Figure 11 – *continued*

(Mutschke et al. 1998; Speck et al. 2000; Heras & Hony 2005; Verhoelst et al. 2009). In these models, gehlenite was included to fit the short-wavelength component of the 10-μm feature and to provide additional flux in the 19-μm region. We find that the 10-μm feature in our sample is fitted reasonably well using a combination of Mg-rich silicates and alumina; thus, the contribution from other dust species can only be small. This discrepancy may be due to the choice of optical constants used for the amorphous silicates.

Two sources in our sample, IRAS 04544−6849 (SSID 4076–4081) and HV 2446 (SSID 4324–4329), have been observed with

Downloaded from http://mnras.oxfordjournals.org/ at Cornell University Library on April 16, 2016

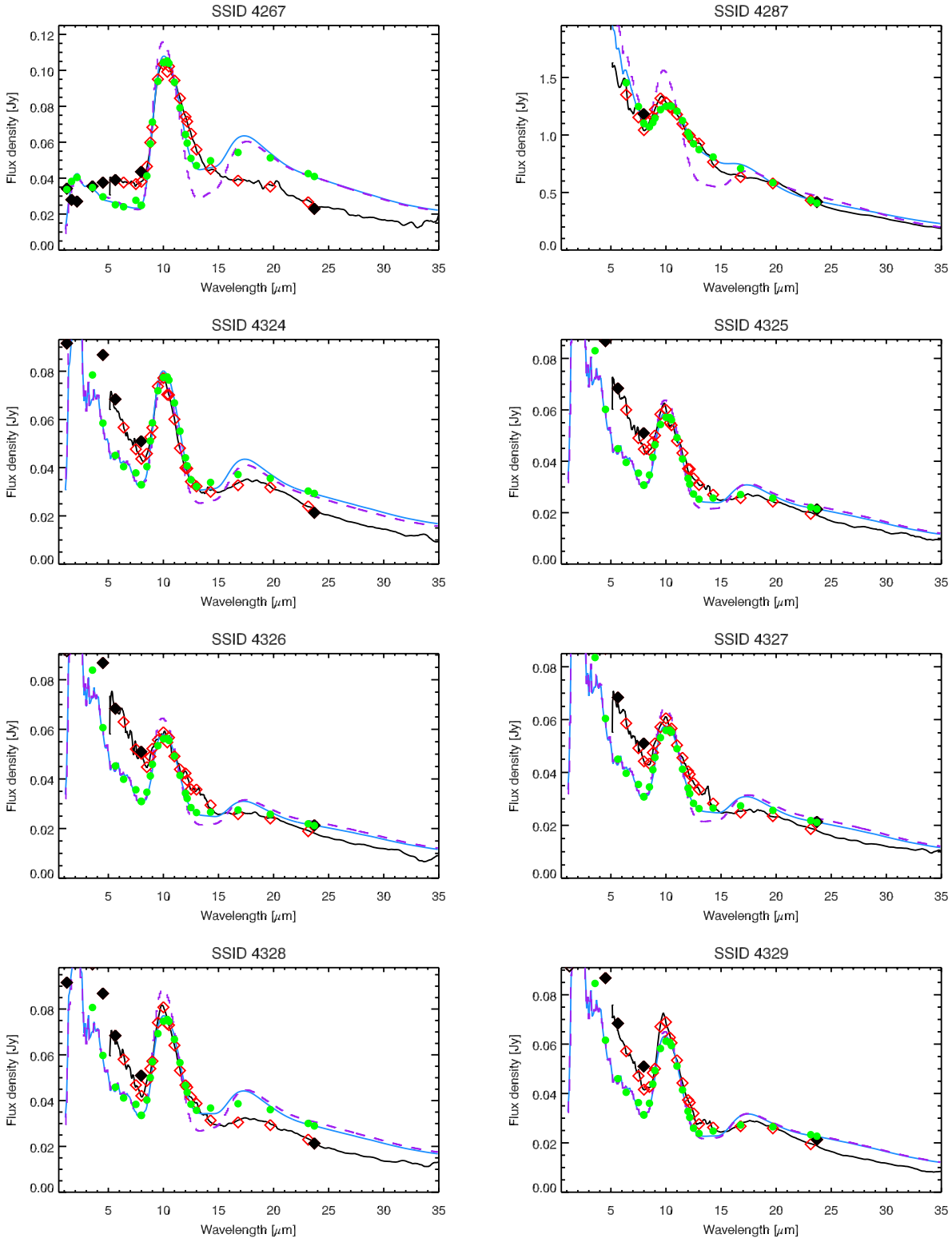

Figure 11 – *continued*

the IRS at different epochs over one variability cycle. The SED for each source includes photometry from multiple epochs, while the spectra represent an instantaneous view of the star at a precise phase of the pulsation cycle. In both these stars, the strength ratio of the 10- to 20-μm SE features varies with pulsation phase (Fig. 14). This is due to changes in the dust temperature, which is directly related to the luminosity of the star (Monnier, Geballe & Danchi 1998). For both these sources, the stellar and dust-shell parameters of our best-fitting models are consistent across the pulsation cycle, as to some extent temporal variations are minimized. However, our

Downloaded from http://mnras.oxfordjournals.org/ at Cornell University Library on April 16, 2016

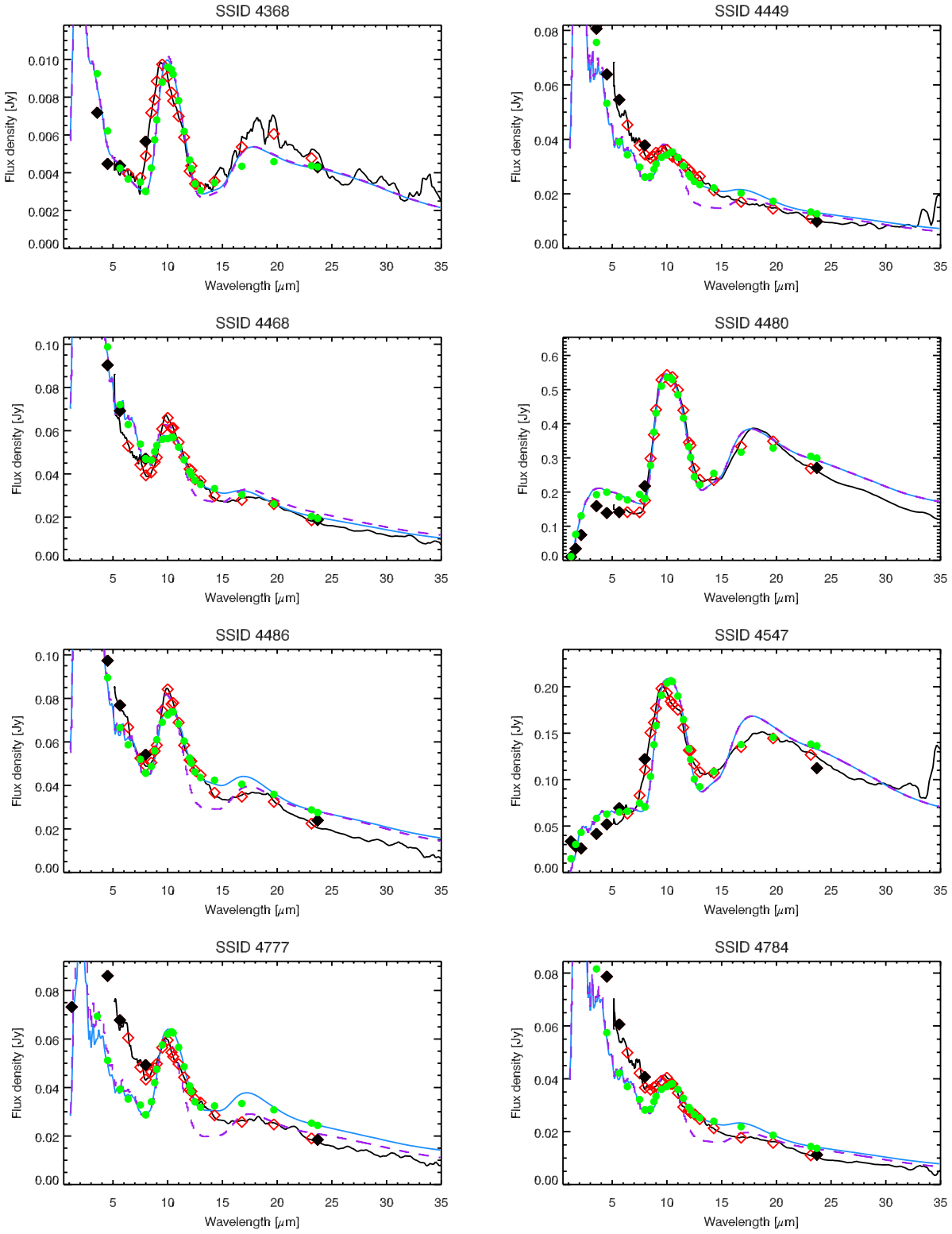

Figure 11 – *continued*

models are sensitive to the change in dust optical properties, as the peak wavelength and width of the 10-μm feature in the spectra show discernible variations between maximum and minimum light in the pulsation cycle; this indicates that the dust properties in the shell vary with the pulsation phase. Furthermore, it will introduce some scattering in our model results when comparing between stars.

The brightest star in the sample, RS Men (SSID 4287), has a bolometric magnitude in excess of −10.78 if it was at the distance of the LMC, which is significantly above the luminosity expected

Downloaded from http://mnras.oxfordjournals.org/ at Cornell University Library on April 16, 2016

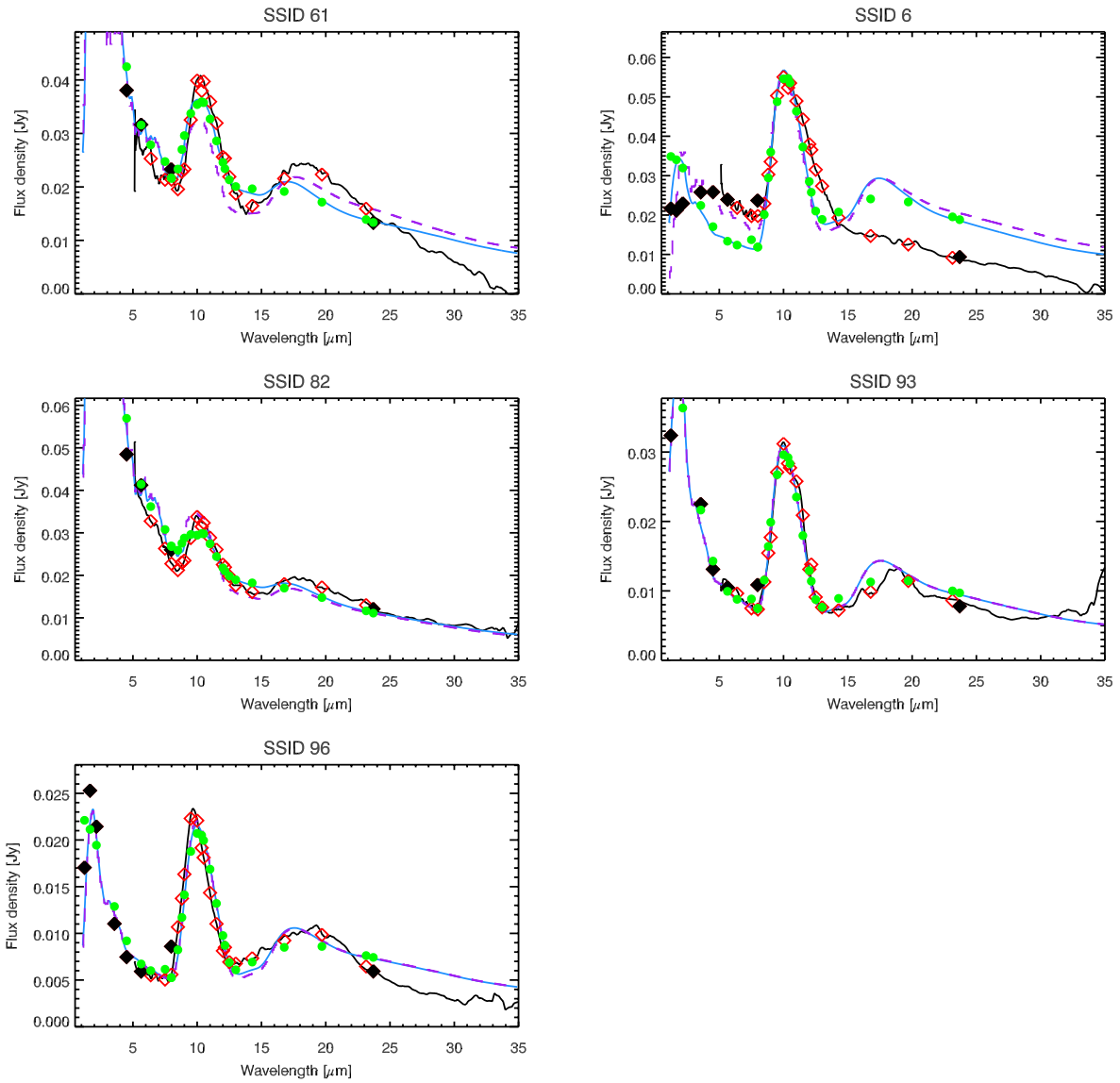

Figure 11 – *continued*

for a bright RSG. This star has been identified as a foreground Mira variable with a distance of 4.75 kpc and radial velocity of 140 km s^{-1} (Whitelock et al. 1994; Buchanan et al. 2006). Incidentally, this source also has the highest alumina fraction in our sample of 60 per cent.

SSID 6 along with SSID 4267 are not well described by our models and their fits are the least satisfactory. These spectra are unusual as they exhibit a strong 10-μm silicate feature but no 18-μm feature. One possible explanation is that the silicates have recently formed and the 18-μm feature has a low contrast ratio with respect to the 10-μm feature. Alternatively, this may be explained by a lack of cooler dust, or the dust may be composed only of small 0.1 μm Mg-rich olivine and alumina grains (Gielen et al. 2011).

5 DISCUSSION

Using the dust-shell models presented here, we are able to constrain both the mass-loss rate and the fractional abundance of alumina. Based on the best-fitting models, the mass-loss rates range from $\sim 8 \times 10^{-8}$ to $5 \times 10^{-6}\,M_{\odot}\,yr^{-1}$, and the alumina fraction ranges from 0 to 50 per cent. In Fig. 15, we compare our derived mass-loss rates to those determined from SED fitting with the GRAMS model in Riebel et al. (2012) and to values listed in Groenewegen et al. (2009). The agreement is generally quite good between our mass-loss rates and the literature values; however, our mass-loss rates are slightly lower than the GRAMS fits, predominantly due to the inclusion of metallic iron grains and alumina in our models.

To have a better understanding of the mass-loss rates and dust abundances derived by this fitting, some limitations of the models must be kept in mind. The photospheric models used are appropriate for solar metallicities and may not be entirely representative of the molecular abundances typical of AGB stars in the Magellanic Clouds. This is more significant for stars with a very low contrast dust excess (MLR $\lesssim 5 \times 10^{-8}\,M_{\odot}\,yr^{-1}$), where there is a strong photospheric contribution and molecular absorption features due to CO, H_2O and SiO are prominent. Observing the CO emission lines in the submillimetre (due to rotational transitions) for a number

Downloaded from http://mnras.oxfordjournals.org/ at Cornell University Library on April 16, 2016

Table 2. The best-fitting model results for the spectra and photometry.

SSID	Spectral type	$M_{\rm bol}$	$R_{\rm in}$ ($R_{\rm star}$)	$\dot{M}$ ($\rm M_\odot\ yr^{-1}$)	Alx. (%)	χ^2_ν	χ^2_ν No alumina
6	M1	-4.69 ± 0.43	15 ± 2.5	$(2.77 \pm 0.74) \times 10^{-7}$	15 ± 10	100.2	97.2
22	M9	-4.10 ± 0.26	2.5 ± 0.5	$(1.41 \pm 0.52) \times 10^{-7}$	30 ± 10	10.3	11.0
38	M5	-5.45 ± 0.36	5.0 ± 0.5	$(3.92 \pm 0.39) \times 10^{-7}$	5 ± 10	6.4	6.6
61	M9	-5.59 ± 0.19	3.0 ± 0.5	$(1.40 \pm 0.28) \times 10^{-7}$	35 ± 10	9.8	15.0
82	M9	-5.99 ± 0.22	7.5 ± 2.5	$(1.26 \pm 0.28) \times 10^{-7}$	40 ± 15	9.4	12.8
93	M1	-4.97 ± 0.07	15 ± 2.5	$(1.05 \pm 0.11) \times 10^{-7}$	0 ± 10	10.0	9.6
96	M5	-4.03 ± 0.22	7.5 ± 2.5	$(1.36 \pm 0.37) \times 10^{-7}$	5 ± 5	14.1	13.7
165	M9	-6.43 ± 0.11	5.0 ± 2.0	$(6.17 \pm 1.13) \times 10^{-7}$	0 ± 10	7.3	7.0
180	M9	-6.01 ± 0.28	2.5 ± 2.0	$(8.48 \pm 4.08) \times 10^{-8}$	40 ± 20	5.2	8.5
182	M1	-3.24 ± 0.31	15 ± 0.5	$(1.42 \pm 0.41) \times 10^{-7}$	10 ± 10	27.0	27.0
182*	M5	-3.29 ± 0.11	5.0 ± 2.5	$(1.45 \pm 0.50) \times 10^{-7}$	15 ± 15	11.6	
4038	M5	-6.96 ± 0.74	7.5 ± 2.5	$(2.63 \pm 0.52) \times 10^{-6}$	20 ± 10	9.7	12.9
4054	M9	-2.57 ± 0.83	7.5 ± 2.5	$(6.94 \pm 0.43) \times 10^{-7}$	30 ± 10	21.8	22.3
4076	M9	-5.92 ± 0.10	5.0 ± 2.0	$(1.22 \pm 0.10) \times 10^{-6}$	5 ± 10	7.3	7.4
4077	M9	-5.91 ± 0.10	5.0 ± 2.0	$(1.22 \pm 0.11) \times 10^{-6}$	5 ± 10	6.7	6.7
4078	M5	-5.91 ± 0.10	7.5 ± 2.5	$(1.21 \pm 0.10) \times 10^{-6}$	0 ± 10	15.4	14.8
4079	M9	-5.91 ± 0.10	5.0 ± 2.0	$(1.22 \pm 0.24) \times 10^{-6}$	0 ± 10	6.4	6.1
4080	M9	-5.98 ± 0.13	5.0 ± 2.5	$(1.26 \pm 0.22) \times 10^{-6}$	0 ± 10	9.0	8.6
4081	M9	-5.93 ± 0.11	5.0 ± 2.5	$(1.23 \pm 0.24) \times 10^{-6}$	0 ± 10	7.1	6.8
4149	M1	-5.76 ± 0.13	15 ± 0.5	$(3.02 \pm 0.97) \times 10^{-6}$	15 ± 25	9.7	11.7
4205	M9	-5.84 ± 0.26	2.5 ± 2.0	$(7.85 \pm 3.76) \times 10^{-8}$	40 ± 20	6.5	10.7
4245	M5	-4.02 ± 0.99	15 ± 0.5	$(1.36 \pm 0.39) \times 10^{-6}$	30 ± 20	23.8	24.8
4267	M1	-4.80 ± 0.99	15 ± 2.5	$(7.30 \pm 0.96) \times 10^{-7}$	25 ± 10	43.9	48.0
4287	M5	-10.78 ± 0.38	5.0 ± 2.5	$(3.05 \pm 1.64) \times 10^{-7}$	60 ± 10	1.4	4.5
4324	M9	-5.85 ± 0.24	5.0 ± 0.5	$(3.15 \pm 1.36) \times 10^{-7}$	15 ± 10	18.7	18.7
4325	M9	-5.92 ± 0.20	2.5 ± 2.5	$(1.63 \pm 0.41) \times 10^{-7}$	15 ± 15	20.1	20.7
4326	M9	-5.94 ± 0.19	2.5 ± 0.5	$(1.64 \pm 0.42) \times 10^{-7}$	20 ± 15	23.9	25.4
4327	M9	-5.93 ± 0.20	2.5 ± 2.0	$(1.64 \pm 0.41) \times 10^{-7}$	20 ± 15	21.6	22.7
4328	M9	-5.89 ± 0.22	5.0 ± 2.5	$(3.21 \pm 1.26) \times 10^{-7}$	25 ± 10	20.3	23.0
4329	M9	-5.94 ± 0.19	2.5 ± 2.0	$(1.64 \pm 0.42) \times 10^{-7}$	5 ± 10	18.0	17.5
4368	M5	-3.67 ± 0.40	2.5 ± 2.5	$(5.79 \pm 1.08) \times 10^{-8}$	5 ± 10	20.2	19.5
4449	M9	-5.88 ± 0.26	3.0 ± 0.5	$(1.20 \pm 0.38) \times 10^{-7}$	50 ± 20	16.2	21.9
4468	M9	-6.56 ± 0.21	2.5 ± 2.5	$(1.09 \pm 0.11) \times 10^{-7}$	40 ± 15	9.1	11.9
4480	M5	-6.11 ± 0.11	15 ± 0.5	$(5.32 \pm 1.20) \times 10^{-6}$	35 ± 25	46.5	44.6
4486	M9	-6.40 ± 0.22	3.0 ± 0.5	$(2.03 \pm 0.35) \times 10^{-7}$	40 ± 15	6.8	10.4
4547	M9	-5.24 ± 0.70	15 ± 0.5	$(3.56 \pm 1.04) \times 10^{-6}$	0 ± 20	27.1	26.0
4777	M9	-5.73 ± 0.10	5.0 ± 0.5	$(2.98 \pm 1.27) \times 10^{-7}$	30 ± 15	33.6	34.5
4784	M9	-5.96 ± 0.25	3.0 ± 0.5	$(1.24 \pm 0.40) \times 10^{-7}$	50 ± 20	19.9	20.9

Note. The best fit obtained without a metallic iron component is indicated by an *.

of Magellanic Cloud sources would also be beneficial to constrain the mass-loss parameters. This would enable us to have a better understanding of the expansion velocity and gas-to-dust ratios in the envelopes of evolved stars. The fits to the sources may also be improved by including a finer grid spacing, for instance, the iron abundance could be incremented in 1 per cent intervals (up to abundances of 10 per cent) to improve the fit to the stars in the near-IR region.

In our sample, the dust composition is best fitted by amorphous silicates, with appreciable amounts of amorphous alumina and additional, small contributions from metallic iron. Alumina is detected in most sources; however, in all cases its fractional abundance is less than 50 per cent. The alumina fractions we have obtained are consistent with those estimated using other methods (see Sections 3.1 and 3.2).

Fig. 16 shows the fractional abundance of alumina plotted against the mass-loss rate. As noted by other authors (Heras & Hony 2005; Blommaert et al. 2006; Lebzelter et al. 2006), there is a correlation between the dust composition and mass-loss rate; the lower the mass-loss rate the higher the percentage of alumina in the shell.

Stars in the early stages of the AGB phase tend to be less luminous and have lower mass-loss rates than their more evolved counterparts. This makes reliable determination of the dust composition challenging, especially for spectra with a low signal-to-noise ratio or with a low-contrast dust excess. AGB stars dominated by alumina dust tend to have mass-loss rates below $10^{-7}\ \rm M_\odot\ yr^{-1}$ (Blommaert et al. 2006). Indeed, the SEDs of a large fraction of Galactic bulge sources in this mass-loss range can be fitted solely with amorphous alumina. The oxygen-rich AGB stars in our LMC sample, which show a DEC, tend to be more luminous, with $M_{\rm init}$ of $\sim$5 $\rm M_\odot$. Our sample is dominated by stars with mass-loss rates between 10^{-7} and $5 \times 10^{-6}\ \rm M_\odot\ yr^{-1}$. These stars display dust components which are from the more advanced stages of the dust condensation sequence, indicated by the low percentage of alumina dust. It should therefore come as no surprise that silicates are the dominant dust type in the present sample. Metallicity effects on the dust-formation efficiency in oxygen-rich stars may also be important.

Future telescopes such as the *JWST* and *SPICA* will be able to obtain high-quality spectra of low mass-loss rate, low-luminosity AGB stars in the Magellanic Clouds and other resolved stellar

Downloaded from http://mnras.oxfordjournals.org/ at Cornell University Library on April 16, 2016

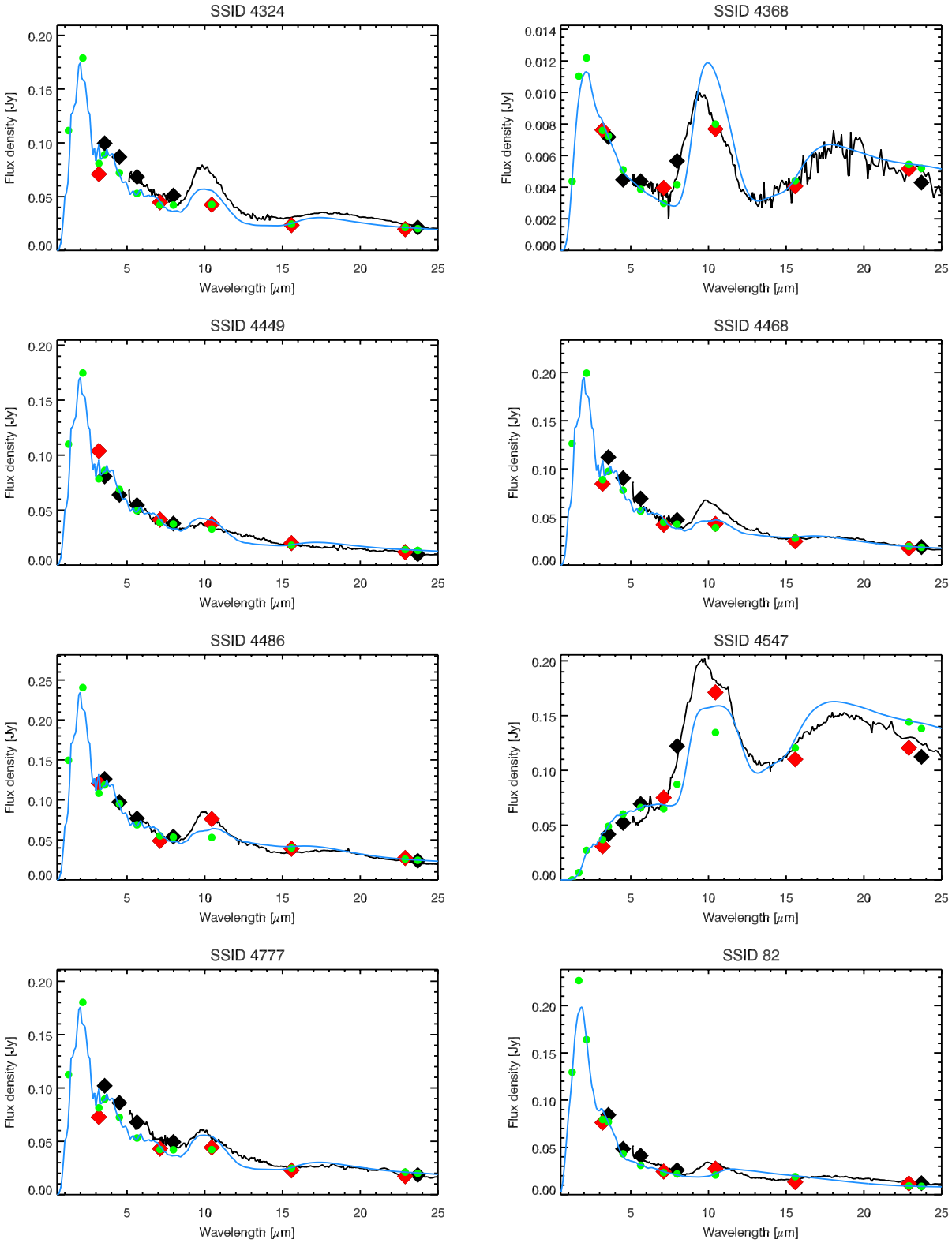

Figure 12. The observed *Spitzer* spectra of O-rich AGB stars (black) and the corresponding best-fitting model (blue). The SAGE photometry is shown as black diamonds, the *AKARI* data as red diamonds and the synthetic flux from the models are shown as green circles. The least-squares fit is performed by matching the green model points to the red/black photometric data points. The spectra are shown only for illustration purposes.

Downloaded from http://mnras.oxfordjournals.org/ at Cornell University Library on April 16, 2016

Table 3. The best-fitting SED model results.

SSID	Spectral type	M_{bol}	R_{in} (R_{star})	$\dot{M}$ ($M_\odot$ yr^{-1})	Alx. (%)	χ^2_ν
82	M5	-6.43 ± 0.08	5.0 ± 2.0	$(6.17 \pm 0.95) \times 10^{-8}$	100 ± 25	21.7
4324	M9	-6.24 ± 0.03	7.5 ± 2.0	$(1.89 \pm 0.38) \times 10^{-7}$	0 ± 20	33.6
4368	M1	-3.10 ± 0.25	2.5 ± 0.5	$(8.89 \pm 2.23) \times 10^{-8}$	0 ± 15	22.4
4449	M9	-6.21 ± 0.01	5.0 ± 0.5	$(9.29 \pm 0.16) \times 10^{-8}$	0 ± 20	4.8
4468	M9	-6.36 ± 0.02	7.5 ± 2.5	$(1.99 \pm 0.14) \times 10^{-7}$	50 ± 25	18.3
4486	M9	-6.56 ± 0.04	5.0 ± 0.5	$(2.18 \pm 0.13) \times 10^{-7}$	60 ± 20	14.1
4547	M9	-4.97 ± 0.14	15.0 ± 0.5	$(5.25 \pm 0.39) \times 10^{-6}$	5 ± 25	35.7
4777	M9	-6.25 ± 0.03	7.5 ± 2.5	$(1.89 \pm 0.15) \times 10^{-7}$	5 ± 25	28.6

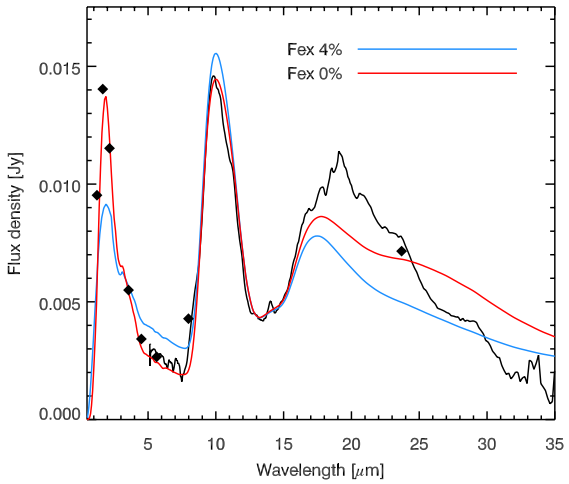

Figure 13. Fits to the SEDs and IRS spectra of SSID 182, using metallic iron (blue) and without iron (red). This is the only source where the fit is not improved with an iron component. The best-fitting model obtained from our grid with 4 per cent iron grains has a χ^2 of 27.0, while the best fit without iron had a χ^2 of 11.6.

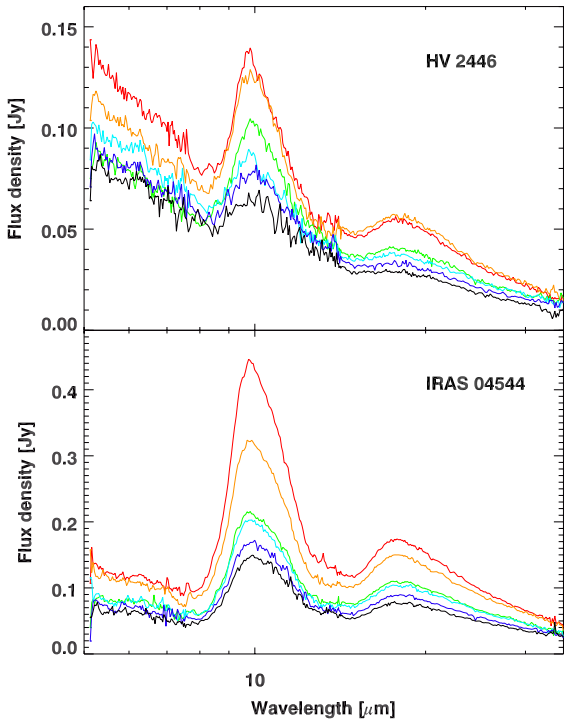

Figure 14. Observed spectral variations for HV 2446 (SSID 4324–4329) and IRAS 04544−6849 (SSID 4076–4081).

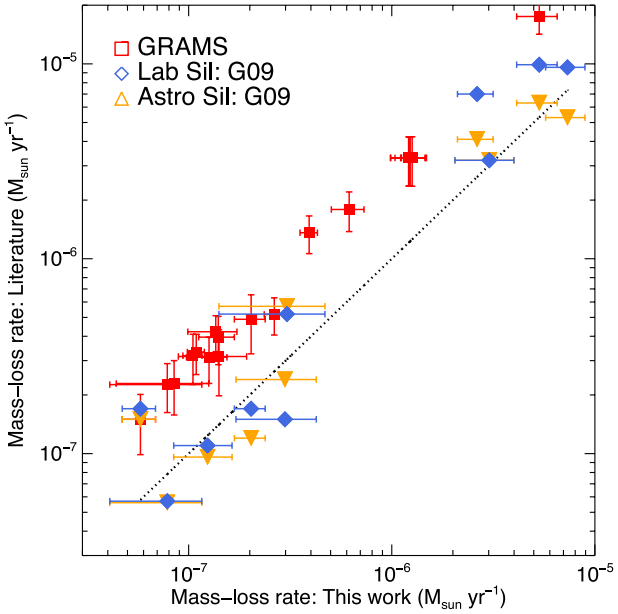

Figure 15. Comparison of mass-loss rate derived in this work with objects in common with our sample from Groenewegen et al. (2009) and the GRAMS model results from Riebel et al. (2012).

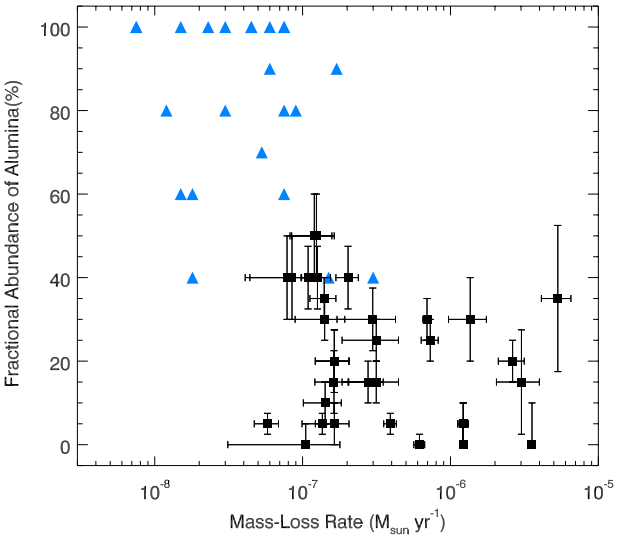

Figure 16. The fractional abundance of alumina in the dust shell of LMC O-AGB stars as a function of mass-loss rate (black squares). Based on Spearman's ρ statistics, the correlation coefficient for the LMC sources is −0.41 with a significance value of 0.01. For comparison, the blue triangles show the distribution of Galactic bulge O-AGB sources from Blommaert et al. (2006).

Downloaded from http://mnras.oxfordjournals.org/ at Cornell University Library on April 16, 2016

populations, eliminating the observational bias towards silicate-rich stars in the current sample. We expect these stars to contain a high percentage of alumina-rich dust.

6 CONCLUSIONS

We have presented a grid of dust radiative transfer models which explores a range of alumina and silicate dust compositions, and stellar and dust-shell parameters. The models have been used to simultaneously fit the spectra and broad-band SED of 37 oxygen-rich AGB stars in the LMC with optically thin circumstellar envelopes. The mass-loss rates of our sample range from $\sim 8 \times 10^{-8}$ to $5 \times 10^{-6}\,\mathrm{M}_{\odot}\,\mathrm{yr}^{-1}$. We find that a combination of amorphous silicates, amorphous alumina and metallic iron provides a good fit to the spectra. All our sources were found to be silicate-rich, though alumina and iron is often present in significant amounts. This dust composition is consistent with the thermodynamic dust condensation sequence for oxygen-rich AGB stars. Furthermore, we show from dust models that the *AKARI* [11]–[15] versus [3.2]–[7] colour is able to determine the fractional abundance of alumina in oxygen-rich AGB stars.

ACKNOWLEDGEMENTS

We would like to thank Ben Sargent for his advice on the silicate dust optical constants. OJ acknowledges the support of an STFC studentship and thanks ASIAA for their support and hospitality during the completion of part of this work. FK acknowledges support from the National Science Council under grant number NSC100-2112-M-001-023-MY3. This work is based on observations made with the *Spitzer* Space Telescope, which is operated by the Jet Propulsion Laboratory, California Institute of Technology under NASA contract 1407, and has made use of the SIMBAD and VizieR data bases, CDS, Strasbourg, France.

REFERENCES

Begemann B., Dorschner J., Henning T., Mutschke H., Guertler J., Koempe C., Nass R., 1997, ApJ, 476, 199
Bloecker T., 1995, A&A, 297, 727
Blommaert J. A. D. L. et al., 2006, A&A, 460, 555
Blum R. D. et al., 2006, AJ, 132, 2034
Bohren C. F., Huffman D. R., 1983, in Bohren C. F., Huffman D. R., eds, Absorption and Scattering of Light by Small Particles. Wiley, New York
Bouwman J., de Koter A., van den Ancker M. E., Waters L. B. F. M., 2000, A&A, 360, 213
Bouwman J., Meeus G., de Koter A., Hony S., Dominik C., Waters L. B. F. M., 2001, A&A, 375, 950
Bowen G. H., Willson L. A., 1991, ApJ, 375, L53
Boyer M. L. et al., 2012, ApJ, 748, 40
Buchanan C. L., Kastner J. H., Forrest W. J., Hrivnak B. J., Sahai R., Egan M., Frank A., Barnbaum C., 2006, AJ, 132, 1890
Cami J., 2002, PhD thesis, Univ. Amsterdam
de Vries B. L., Min M., Waters L. B. F. M., Blommaert J. A. D. L., Kemper F., 2010, A&A, 516, A86
Demyk K., Dartois E., Wiesemeyer H., Jones A. P., d'Hendecourt L., 2000, A&A, 364, 170
Dijkstra C., Speck A. K., Reid R. B., Abraham P., 2005, ApJ, 633, L133
Dorschner J., Begemann B., Henning T., Jaeger C., Mutschke H., 1995, A&A, 300, 503
Draine B. T., Lee H. M., 1984, ApJ, 285, 89
Egan M. P., Van Dyk S. D., Price S. D., 2001, AJ, 122, 1844
Feautrier P., 1964, C. R. Acad. Sci., Paris, 258, 3189
Fluks M. A., Plez B., The P. S., de Winter D., Westerlund B. E., Steenman H. C., 1994, A&AS, 105, 311
Gail H.-P., 2010, in Henning T., ed., Lecture Notes in Physics, Vol. 815, Astromineralogy. Springer, Berlin, p. 61
Gail H., Sedlmayr E., 1999, A&A, 347, 594
Gielen C. et al., 2011, A&A, 533, A99
Groenewegen M. A. T., 2006, A&A, 448, 181
Groenewegen M. A. T., Sloan G. C., Soszyński I., Petersen E. A., 2009, A&A, 506, 1277
Habing H. J., Olofsson H., eds, 2003, Asymptotic Giant Branch Stars. Springer, Berlin, p. 8
Hackwell J. A., 1972, A&A, 21, 239
Heras A. M., Hony S., 2005, A&A, 439, 171
Höfner S., 2007, in Kerschbaum F., Charbonnel C., Wing R. F., eds, ASP Conf. Ser. Vol. 378, Why Galaxies Care About AGB Stars: Their Importance as Actors and Probes. Astron. Soc. Pac., San Francisco, p. 145
Höfner S., 2008, A&A, 491, L1
Hron J., Aringer B., Kerschbaum F., 1997, A&A, 322, 280
Ita Y. et al., 2008, PASJ, 60, 435
Ivezic Z., Elitzur M., 1995, ApJ, 445, 415
Ivezic Z., Elitzur M., 1997, MNRAS, 287, 799
Jäger C., Fabian D., Schrempel F., Dorschner J., Henning Th., Wesch W., 2003, A&A, 401, 57
Jones O. C. et al., 2012, MNRAS, 427, 3209
Kastner J. H., Thorndike S. L., Romanczyk P. A., Buchanan C. L., Hrivnak B. J., Sahai R., Egan M., 2008, AJ, 136, 1221
Kato D. et al., 2012, AJ, 144, 179
Kemper F., Waters L. B. F. M., de Koter A., Tielens A. G. G. M., 2001, A&A, 369, 132
Kemper F., de Koter A., Waters L. B. F. M., Bouwman J., Tielens A. G. G. M., 2002, A&A, 384, 585
Kemper F. et al., 2010, PASP, 122, 683
Koike C., Kaito C., Yamamoto T., Shibai H., Kimura S., Suto H., 1995, Icarus, 114, 203
Kučinskas A. et al., 2005, A&A, 442, 281
Kučinskas A., Hauschildt P. H., Brott I., Vansevičius V., Lindegren L., Tanabé T., Allard F., 2006, A&A, 452, 1021
Lebzelter T., Posch T., Hinkle K., Wood P. R., Bouwman J., 2006, ApJ, 653, L145
Little-Marenin I. R., Little S. J., 1990, AJ, 99, 1173
Marshall J. R., van Loon J. T., Matsuura M., Wood P. R., Zijlstra A. A., Whitelock P. A., 2004, MNRAS, 355, 1348
Mathis J. S., Rumpl W., Nordsieck K. H., 1977, ApJ, 217, 425
McDonald I., Sloan G. C., Zijlstra A. A., Matsunaga N., Matsuura M., Kraemer K. E., Bernard-Salas J., Markwick A. J., 2010, ApJ, 717, L92
Min M., Hovenier J. W., de Koter A., 2003, A&A, 404, 35
Monnier J. D., Geballe T. R., Danchi W. C., 1998, ApJ, 502, 833
Mutschke H., Begemann B., Dorschner J., Guertler J., Gustafson B., Henning Th., Stognienko R., 1998, A&A, 333, 188
Norris B. R. M. et al., 2012, Nature, 484, 220
Olofsson H., 2004, in Habing H. J., Olofsson H., eds, Asymptotic Giant Branch Stars. Springer, Berlin, p. 325
Onaka T., de Jong T., Willems F. J., 1989, A&A, 218, 169
Ordal M. A., Bell R. J., Alexander R. W., Jr, Newquist L. A., Querry M. R., 1988, Appl. Opt., 27, 1203
Ossenkopf V., Henning T., Mathis J. S., 1992, A&A, 261, 567
Pietrzyński G. et al., 2013, Nature, 495, 76
Posch T., Kerschbaum F., Mutschke H., Dorschner J., Jäger C., 2002, A&A, 393, L7
Riebel D., Srinivasan S., Sargent B., Meixner M., 2012, ApJ, 753, 71
Sargent B. A. et al., 2010, ApJ, 716, 878
Sargent B. A., Srinivasan S., Meixner M., 2011, ApJ, 728, 93
Sloan G. C., Price S. D., 1995, ApJ, 451, 758
Sloan G. C., Price S. D., 1998, ApJS, 119, 141
Sloan G. C., Kraemer K. E., Goebel J. H., Price S. D., 2003, ApJ, 594, 483
Sloan G. C., Kraemer K. E., Wood P. R., Zijlstra A. A., Bernard-Salas J., Devost D., Houck J. R., 2008, ApJ, 686, 1056

Downloaded from http://mnras.oxfordjournals.org/ at Cornell University Library on April 16, 2016

Sloan G. C. et al., 2010, ApJ, 719, 1274
Sogawa H., Kozasa T., 1999, ApJ, 516, L33
Speck A. K., Barlow M. J., Sylvester R. J., Hofmeister A. M., 2000, A&AS, 146, 437
Srinivasan S., Sargent B. A., Meixner M., 2011, A&A, 532, A54
Stencel R. E., Nuth J. A., III, Little-Marenin I. R., Little S. J., 1990, ApJ, 350, L45
Suh K.-W., 1999, MNRAS, 304, 389
Tielens A. G. G. M., 1990, in Mennessier M. O., Omont A., eds, From Miras to Planetary Nebulae: Which Path for Stellar Evolution? Editions Frontieres, Gif-sur-Yvette, p. 186
Treffers R., Cohen M., 1974, ApJ, 188, 545
Ueta T., Meixner M., 2003, ApJ, 586, 1338
van Loon J. T., Zijlstra A. A., Bujarrabal V., Nyman L.-Å., 2001, A&A, 368, 950
Vassiliadis E., Wood P. R., 1993, ApJ, 413, 641
Verhoelst T., van der Zypen N., Hony S., Decin L., Cami J., Eriksson K., 2009, A&A, 498, 127
Whitelock P., Menzies J., Feast M., Marang F., Carter B., Roberts G., Catchpole R., Chapman J., 1994, MNRAS, 267, 711
Whitelock P. A., Feast M. W., van Loon J. T., Zijlstra A. A., 2003, MNRAS, 342, 86
Wood P. R., Whiteoak J. B., Hughes S. M. G., Bessell M. S., Gardner F. F., Hyland A. R., 1992, ApJ, 397, 552
Woods P. M. et al., 2011, MNRAS, 411, 1597
Woolf N. J., Ney E. P., 1969, ApJ, 155, L181
Wright E. L. et al., 2010, AJ, 140, 1868

APPENDIX A

In Fig. A1, we show CCD of the model grid compared to all the evolved star candidates in the SAGE LMC sample and the confirmed O-rich and C-rich AGB stars in the SAGE-Spec sample. The O-rich AGB candidates and RSG candidates identified by Blum et al. (2006) are predominantly on the early AGB and have a limited circumstellar excess. Photometrically, the reddest sources (for which our models are optimized) are not included in the O-AGB classification, instead these objects are classified as extreme AGB stars, far-IR objects [which also include young stellar objects (YSOs)] or are missed by the colour cuts. For the faint O-rich AGB stars, the 3σ error in the colours is sufficient to explain the scatter. Table A1 provides the average photometry in each band and the spectral classification of all the O-rich sources used in this study.

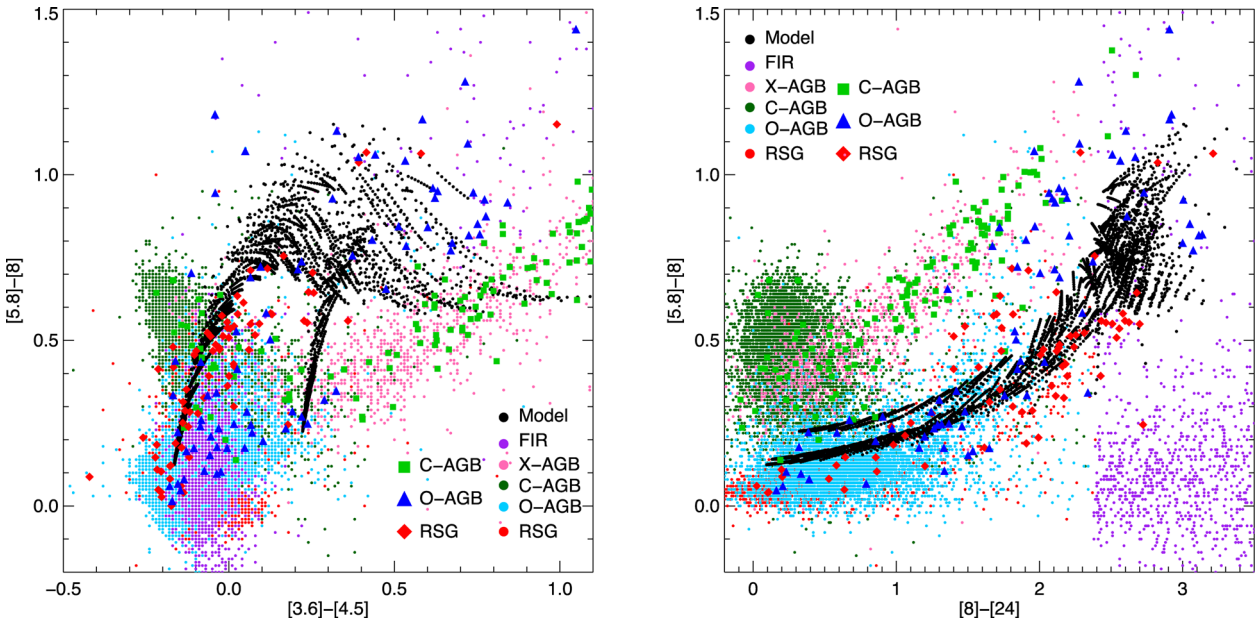

Figure A1. *Spitzer* IRAC/MIPS CCD showing the evolved stellar population of the LMC and their various photometric classifications, compared to our model grid. The colour of the small points represents the photometric classification of sources in the SAGE data base, and the small black dots denote the models from our O-rich grid. The spectroscopically classified evolved star's symbols are as in Fig. 3.

Table A1. Spectral classification and photometric catalogue of all the O-rich sources used in this study. Magnitudes in this table have not been corrected for reddening. A full version is available in the electronic edition.

SSID	Spectral class	2MASS			IRAC				MIPS	*WISE*				*AKARI*				
		J	*H*	*K*	[3.6]	[4.5]	[5.8]	[8.0]	[24]	*W*1	*W*2	*W*3	*W*4	*N*3	*S*7	*S*11	*L*15	*L*24
1	O-AGB	12.41	11.49	11.19	10.91	10.81	10.69	10.49	9.64	10.96	10.89	10.24	9.35	–	–	–	–	–
4	RSG	10.10	9.27	9.01	8.87	9.04	8.87	8.75	7.55	8.85	9.04	8.46	7.79	–	–	–	–	–
6	O-AGB	12.17	11.71	11.16	10.08	9.60	9.22	8.56	7.20	10.36	9.71	7.51	6.82	–	–	–	–	–
8	O-AGB	14.36	13.15	12.48	11.13	10.61	10.03	9.19	7.22	11.20	10.52	8.42	7.31	–	–	–	–	–

Downloaded from http://mnras.oxfordjournals.org/ at Cornell University Library on April 16, 2016

SUPPORTING INFORMATION

Additional Supporting Information may be found in the online version of this article:

Table A1. Spectral classification and photometric catalogue of all the O-rich sources used in this study. Magnitudes in this table have not been corrected for reddening. A full version is available in the electronic edition.
(http://mnras.oxfordjournals.org/lookup/suppl/doi:10.1093/mnras/stu286/-/DC1).

Please note: Oxford University Press are not responsible for the content or functionality of any supporting materials supplied by the authors. Any queries (other than missing material) should be directed to the corresponding author for the article.

This paper has been typeset from a TEX/LATEX file prepared by the author.

Downloaded from http://mnras.oxfordjournals.org/ at Cornell University Library on April 16, 2016